Mid-infrared time-domain study of recent dust production events in the extreme debris disc of TYC 4209-1322-1

Attila Moór,[1,2]* Péter Ábrahám,[1,2,3] Ágnes Kóspál,[1,2,4,3] Kate Y. L. Su,[5] George H. Rieke,[5,6] Krisztián Vida,[1,2] Gianni Cataldi,[7,8] Attila Bódi,[1,2,9] Zsófia Bognár,[1,2,9] Borbála Cseh,[1,2,10] Géza Csörnyei,[1,2] Nóra Egei,[1,2] Anikó Farkas,[1,2] Ottó Hanyecz,[1,2,11] Bernadett Ignácz,[1,2] Csilla Kalup,[1,2] Réka Könyves-Tóth,[1,2] Levente Kriskovics,[1,2] László Mészáros,[1,2] András Pál,[1,2] András Ordasi,[1,2] Krisztián Sárneczky,[1,2] Bálint Seli,[1,2,12] Ádám Sódor,[1,2,9] Róbert Szakáts,[1,2] József Vinkó[1,2,13] and Gabriella Zsidi[1,2]

[1] *Konkoly Observatory, Research Centre for Astronomy and Earth Sciences, Eötvös Loránd Research Network (ELKH), Konkoly-Thege Miklós út 15-17, H-1121 Budapest, Hungary*
[2] *CSFK, MTA Centre of Excellence, Budapest, Konkoly Thege Miklós út 15-17., H-1121, Hungary*
[3] *ELTE Eötvös Loránd University, Institute of Physics, Pázmány Péter sétány 1/A, 1117 Budapest, Hungary*
[4] *Max-Planck-Institut für Astronomie, Königstuhl 17, D-69117 Heidelberg, Germany*
[5] *Department of Astronomy/Steward Observatory, The University of Arizona, Tucson, AZ 85721-0009, USA*
[6] *Department of Planetary Sciences/Lunar & Planetary Laboratory, The University of Arizona, 1629 E University Blvd, Tucson AZ 85721-0092, USA*
[7] *National Astronomical Observatory of Japan, Osawa 2-21-1, Mitaka, Tokyo 181-8588, Japan*
[8] *Department of Astronomy, Graduate School of Science, The University of Tokyo, Tokyo 113-0033, Japan*
[9] *MTA CSFK Lendület Near-Field Cosmology Research Group*
[10] *MTA-ELTE Lendület "Momentum" Milky Way Research Group, Hungary*
[11] *Faculty of Informatics, Eötvös Loránd University, Budapest, Hungary*
[12] *Eötvös University, Department of Astronomy, Pf. 32, 1518 Budapest, Hungary*
[13] *Department of Optics and Quantum Electronics, University of Szeged, Dóm tér 9, H-6720 Szeged, Hungary*

ABSTRACT

Extreme debris discs are characterized by unusually strong mid-infrared excess emission, which often proves to be variable. The warm dust in these discs is of transient nature and is likely related to a recent giant collision occurring close to the star in the terrestrial region. Here we present the results of a 877 days long, gap-free photometric monitoring performed by the *Spitzer Space Telescope* of the recently discovered extreme debris disc around TYC 4209-1322-1. By combining these observations with other time-domain optical and mid-infrared data, we explore the disc variability of the last four decades, with particular emphasis on the last 12 years. During the latter interval the disc showed substantial changes, the most significant was the brightening and subsequent fading between 2014 and 2018 as outlined in *WISE* data. The *Spitzer* light curves outline the fading phase and a subsequent new brightening of the disc after 2018, revealing an additional flux modulation with a period of ∼39 days on top of the long-term trend. We found that all these variations can be interpreted as the outcome of a giant collision that happened at an orbital radius of ∼0.3 au sometime in 2014. Our analysis implies that a collision on a similar scale could have taken place around 2010, too. The fact that the disc was already peculiarly dust rich 40 years ago, as implied by *IRAS* data, suggests that these dust production events belong to a chain of large impacts triggered by an earlier even more catastrophic collision.

Key words: (stars:) circumstellar matter – infrared: planetary systems – stars: individual: TYC 4209-1322-1

1 INTRODUCTION

We know that 20–30% of main-sequence stars exhibit excess emission at infrared (IR) wavelengths, implying the presence of an optically thin circumstellar dust disc heated by the stellar light (Su et al. 2006; Trilling et al. 2008; Thureau et al. 2014; Montesinos et al. 2016; Sibthorpe et al. 2018). The short lifetime of such dust grains

implies that they are of second generation, produced via erosion of larger planetesimals, in most cases probably through their steady state collisional grinding (Wyatt 2008). The majority of these debris discs, as we call the ensemble of solids of different sizes together, are comprised of cold material (<100 K) residing at tens to hundreds of astronomical units (au) from the host star (Hughes et al. 2018). These systems can be considered massive analogues of the Solar system's Kuiper-belt. A few tens of per cent of such debris discs also display mid-IR excess (Kennedy & Wyatt 2014) indicating the pres-

---

* E-mail: moor.attila@csfk.org

ence of additional warmer dust material ($\gtrsim$150K), which is likely orbiting closer to the star. Furthermore, there are discs that contain only warm dust (e.g., Ballering et al. 2013). The observed warmer particles can be produced in situ in an inner planetesimal belt, but the sustenance of this dust – at least in part – can also come from an outer, colder planetesimal belt either via sublimation or disruption of comets transported from this outer reservoir or via grains migrated inward under the influence of drag forces (e.g., Kennedy & Piette 2015; Marboeuf et al. 2016).

Mid-IR observations in recent decades have revealed a small but growing number of debris discs – mostly around FGK-type main-sequence stars – that possess peculiarly large amounts of warm dust with temperatures higher than 300 K (e.g., Song et al. 2005; Melis et al. 2010; Zuckerman et al. 2012; Tajiri et al. 2020; Melis et al. 2021; Moór et al. 2021; van den Ancker et al. 2021; Higashio et al. 2022). While in most known debris discs the fraction of the stellar luminosity reradiated by the dust is lower than 10^{-3}, the dust material of these warm *extreme debris discs* (EDDs, Balog et al. 2009) intercepts at least one percent of the stellar light and thermally re-emits it mostly in the mid-IR. These very high fractional luminosities suggest that these discs are at least partly optically thick for the stellar illumination. In addition to their high dust content, EDDs show several features highly uncommon in normal debris systems. They tend to display significant photometric variability at 3–5 μm on monthly to yearly timescales (Meng et al. 2014, 2015; Su et al. 2019; Moór et al. 2021; Su et al. 2022), and have strong mid-IR solid state features, implying the presence of short-lived, small, submicron-sized dust particles (Olofsson et al. 2012). In contrast to typical debris discs, these characteristics cannot be explained by the slow, steady state collisional grinding of an in situ planetesimal belt that started its evolution after the dispersal of the gas-rich initial primordial disc, but instead point to a recent large transient dust production event – likely related to a giant collision – happening within 1–2 au of the star (Jackson & Wyatt 2012; Su et al. 2019).

While semi-annual photometric data from the Wide-field Infrared Survey Explorer (*WISE*; Wright et al. 2010) satellite allow us to get a picture of the annual variations of EDDs at 3.4 and 4.6 μm, dedicated monitoring projects with shorter cadences conducted with the *Spitzer Space Telescope* (*Spitzer*; Werner et al. 2004) made it possible to detect changes that happen over weeks or months. Su et al. (2019) presented the 3.6 and 4.5 μm *Spitzer* light curves of two EDDs, ID 8 and P 1121, both showing complex variations, with shorter, periodic (or quasi-periodic) modulations on top of longer-term trends. By attributing the dust production to recent collisional events, they found that the main features of the observed disc variability, including the periodic modulations, can be explained by the dynamical and collisional evolution of the ejected debris cloud. Their model allowed to constrain some important parameters of the event, such as the location of the collision and the size of the colliding bodies. While the light curve of P 1121 is consistent with a giant impact that occurred prior to the start of the monitoring, the time-domain data of ID 8 suggest at least two recent collisions at different times and locations (Su et al. 2019).

Using the AllWISE infrared photometric catalogue (Cutri & et al. 2013) we have recently discovered a new EDD around TYC 4209-1322-1 (hereafter TYC 4209), a $\sim$275 Myr old G1V type star (Moór et al. 2021) located at 270.8 pc (Gaia Collaboration et al. 2016, 2020; Bailer-Jones et al. 2021). The star has an M3.5-type companion with a projected separation of 22$''$2 ($\sim$6000 au, Moór et al. 2021). TYC 4209 exhibits excess in all four *WISE* bands, between 3.4 and 22 μm, with a fractional luminosity of $L_{disc}/L_* \sim$0.07, which is very high even among EDDs. Based on

multi-epoch photometric data obtained with *WISE* between 2010 and 2020, we found that this disc displayed significant variability at 3.4 and 4.6 μm both on daily and yearly timescales (Moór et al. 2021). By analyzing the observed brightening events, we concluded that they cannot be explained by increasing the dust temperatures solely, but require the formation of new dust material.

In this work we present a more detailed study of this disc and its mid-IR variability using time-domain photometry obtained with the Infrared Array Camera (IRAC; Fazio et al. 2004) of *Spitzer* at 3.6 μm (IRAC1) and 4.5 μm (IRAC2). Located close to the northern ecliptic pole at an ecliptic latitude of 87$°$3, TYC 4209 was in the continuous viewing zone of *Spitzer* allowing a gap-free monitoring over 877 days. The optical variations of the object were also monitored photometrically during the studied period and its spectrum between 2 and 3.8 μm was measured at three epochs using the IRTF/SpeX instrument. We present the data reduction of these new observations in Sect. 2. The analysis of the stellar and disc variability and the determination of the fundamental disc parameters are given in Sect. 3. We interpret the observed disc variability in the framework of current models of giant impacts (Sect. 4). Finally the main outcomes of the study are summarized in Sect. 5.

2 OBSERVATIONS AND DATA REDUCTION

2.1 Spitzer/IRAC multi-epoch imaging at 3.6 and 4.5 μm

IRAC observations of TYC 4209 were performed in programs PID 13161 and PID 14071 (PI: A. Moór) in the post-cryogenic ('warm') phase of the *Spitzer* mission. In the first program, 63 measurements were obtained between 2017-07-01 and 2019-03-14 using an average cadence of $\sim$10 days. The second program started on 2019-04-06 and finished on 2019-11-25. In this, we conducted 48 observations utilizing a denser sampling with an average cadence of $\sim$5 days. The longest gap in the time series ($\sim$23 days) was between the end of the first program and the beginning of the second program. All observations were done in full-array observing mode[1] with exposure times of 1.2 s using a 9-point random dither pattern with medium scale[2].

In our data reduction we used the datasets produced by the Spitzer Science Center (SSC) with the IRAC pipeline version of S19.2.0. These contain both processed images for the nine dither positions (Corrected Basic Calibrated Data, CBCDs) and mosaic images compiled from them. Figure 1 shows the immediate vicinity of TYC 4209 at 4.5 μm. As this mosaic image demonstrates, it appears as a well-separated, bright point source. The photometric analysis was performed on the individual CBCD frames. We used aperture photometry with a radius of 3 pixels (the native pixel size is 1$''$22) to extract flux densities from these data. To estimate the centroid position of our target we employed a first moment box centroider algorithm proposed by the SSC (`box_centroider`[3]). The background was measured in a sky annulus between radii of 12 and 20 pixels using an iterative sigma-clipping method with a clipping threshold of 3σ. For the aperture photometry we utilized the `daophot` package of the Interactive Data Language (IDL) astronomy library (Landsman

---

[1] https://irsa.ipac.caltech.edu/data/SPITZER/docs/irac/iracinstrumenthandbook/

[2] https://irsa.ipac.caltech.edu/data/SPITZER/docs/irac/calibrationfiles/dither/

[3] https://irsa.ipac.caltech.edu/data/SPITZER/docs/dataanalysistools/tools/contributed/irac/box_centroider/
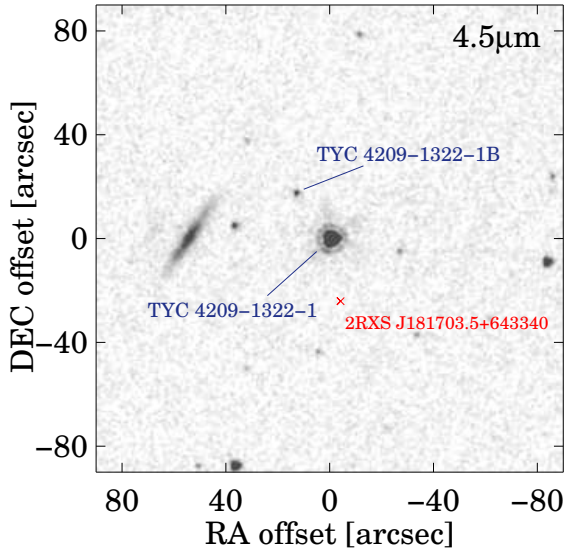
Figure 1. Field of TYC 4209 at 4.5 μm with *Spitzer* (based on data obtained in AOR 63191296).

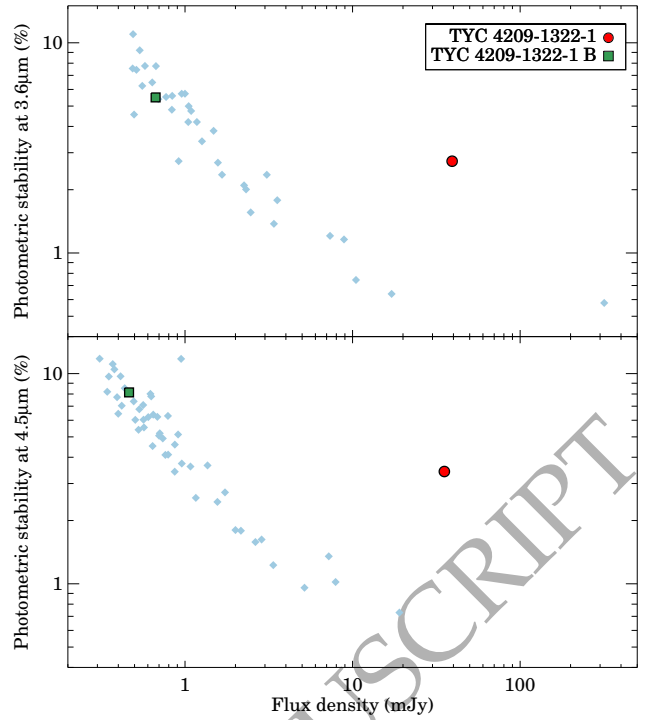**Figure 2.** Photometric stability of TYC 4209 and other sources in its vicinity at 3.6 and 4.5 μm as a function of their flux density in the specific band during the *Spitzer* measurement programme.

1995). The obtained photometry was corrected both for the pixel phase effect and for array location dependent response utilizing the `irac_aphot_corr`[4] task provided by the SSC. We then applied aperture correction using the appropriate correction factors taken from the IRAC Instrument Handbook v3.0.1[5]. The final flux density and its uncertainty were derived by calculating the center and dispersion of the distribution of the nine individual photometric data points obtained at the different dither positions using bisquare weighting (implemented in the `biweight_mean` IDL task[6]). The photometric results are listed in Table 1.

To evaluate the photometric stability during the monitoring programme we constructed the 3.6 and 4.5 μm light curves of nearby objects covered by our observations. Due to the optical design of the IRAC instrument, the IRAC1 and IRAC2 arrays were operated simultaneously providing two nearly adjacent $5'.2 \times 5'.2$ field of views with one covering the target. The nearest edges of the images are separated by $\sim 1'.52$. As the field of view rotated from epoch to epoch, only sources in the immediate vicinity of TYC 4209 were measured at all times. We considered only those objects for which at least 10 measurements were made with a difference of at least two years between the first and last point. The lists of sources are only partially identical in the two bands. Photometry of these additional targets was obtained using the same procedure as described above for TYC 4209, the photometric stability was calculated as the standard deviation of the normalized flux densities. Figure 2 shows the derived photometric stabilities as a function of the flux level for both IRAC channels. At the flux level of TYC 4209 these results suggest a stability better than 0.7% and 1% at 3.6 and 4.5 μm, respectively. TYC 4209 clearly stands out from the trend in both bands, proving that it showed significant changes during the monitoring period. In addition to our main target, at 4.5 μm

[4] https://irsa.ipac.caltech.edu/data/SPITZER/docs/dataanalysistools/tools/contributed/irac/iracphotcorr/
[5] https://irsa.ipac.caltech.edu/data/SPITZER/docs/irac/iracinstrumenthandbook/
[6] https://idlastro.gsfc.nasa.gov/ftp/pro/robust/biweight_mean.pro

Table 1. Spitzer/IRAC Photometry of the TYC 4209 system. The full table of all 111 observations is available in electronic format. From the left- to the right-hand side, the columns correspond to the Astronomical Observing Request (AOR) key of the observation, the Modified Julian Date of the 3.6 μm observation (computed as the mean of the MJDs of the individual frames at the nine dither positions), the measured flux density and its uncertainty at 3.6 μm, the Modified Julian Date of the 4.5 μm observation, the measured flux density and its uncertainty at 4.5 μm.

AOR	MJD$_{3.6}$ (days)	$F_{3.6}$ (mJy)	$\sigma F_{3.6}$ (mJy)	MJD$_{4.5}$ (days)	$F_{4.5}$ (mJy)	$\sigma F_{4.5}$ (mJy)
63183360	57935.93048	39.68	0.11	57935.92921	37.00	0.16
63183616	57946.87000	39.56	0.11	57946.86873	36.67	0.13
63183872	57956.23380	39.14	0.13	57956.23253	35.95	0.11
63184128	57965.70466	39.41	0.10	57965.70339	36.34	0.09
63184384	57975.09877	39.58	0.20	57975.09751	36.21	0.12
63184640	57986.73201	39.01	0.11	57986.73074	35.66	0.10
63184896	57995.04548	38.52	0.12	57995.04421	35.09	0.11
63185152	58005.22230	38.89	0.19	58005.22103	35.42	0.07
63185408	58016.35168	38.94	0.17	58016.35042	35.31	0.08
63185664	58026.34130	38.79	0.14	58026.34004	35.53	0.19

there is another outlying object, WISE J181805.36+642954.6, that is classified as a W UMa type eclipsing binary based on its ASAS-SN optical light curve (Jayasinghe et al. 2018). It is therefore not surprising that this system also proves to be variable in the mid-IR.

Similarly to TYC 4209, its companion was also measured at each epoch. As Fig. 2 demonstrates, data of TYC 4209 B do not imply any significant changes over the observed period. By computing the weighted average of all available 111 photometric data points, for this star we obtained flux densities of 0.66±0.02 mJy and 0.47±0.01 mJy
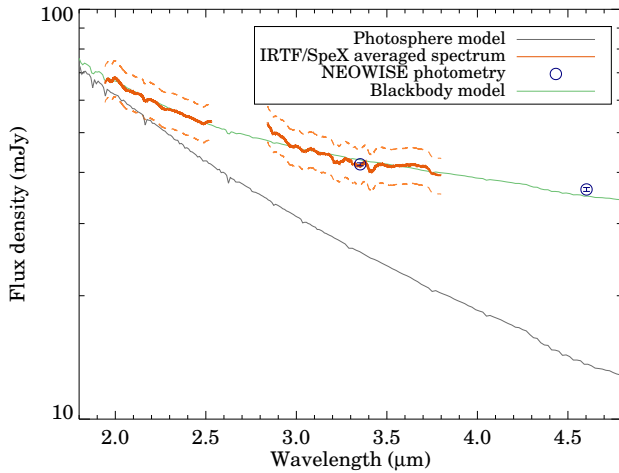
Figure 3. The SpeX/IRTF spectrum of TYC 4209. The plotted spectrum is obtained as the average of three individual spectra (see Sect. 2.3). Flux uncertainties are marked by dashed orange lines, mainly dominated by the 10% systematic instrumental errors. The stellar photosphere model and a blackbody model (with T = 1040 K) fitted to the measured spectrum (Sect. 3.2) are also plotted.

at 3.6 and 4.5 μm, respectively. The quoted uncertainties are calculated by adding quadratically the measurement and absolute calibration uncertainties, where the latter component is assumed to be 2%[7]. In Moór et al. (2021) we derived an effective temperature of 3230±55 K for TYC 4209 B. Assuming that, like the primary component, it has solar metallicity and adopting a log g value of 5.0 dex, we fitted a NextGen atmosphere model to the Gaia EDR3 and 2MASS photometric data of the star. This model predicts photospheric flux densities of 0.68±0.01 mJy and 0.45±0.01 mJy in the IRAC 1 and IRAC 2 bands, respectively, which are consistent with the measured fluxes, i.e., TYC 4209 B shows no excess in these bands.

2.2 WISE multi-epoch photometry

The discovery of the disc around TYC 4209, and the first study of its infrared variations, were based on data obtained with the *WISE* satellite (Moór et al. 2021). Since the start of its mission in 2010, *WISE* has collected data on TYC 4209 in 18 observing windows, with a time shift of ~6 months between them, except for a hibernation period of the telescope, between 2011 and 2013, when no observations were performed. While in the first window, during the cryogenic phase, measurements were made in all four photometric bands available (W1, W2, W3, and W4 at 3.4, 4.6, 12, and 22 μm, respectively), in the subsequent windows, observations were restricted to the two shortest wavelength bands. Thanks to its advantageous position close to the ecliptic pole, for TYC 4209 the observation windows were quite long (with widths of 17–40 days), allowing the telescope to obtain 40–300 individual single exposures in each window. In Moór et al. (2021), after discarding bad quality exposures, we computed the average of the remaining data points in each observing window between 2010 and 2019. The continuation of the NEOWISE Reactivation program (Mainzer et al. 2014) in 2020–21

allowed us to derive 3.4 and 4.6 μm photometry in four additional epochs[8]. These were calculated using the same method as employed in our previous work.

2.3 IRTF/SpeX mid-IR spectroscopy

We observed TYC 4209 three times on 2020 Jun 18, Jul 28 and Aug 16 with the NASA IRTF telescope using the SpeX instrument (Rayner et al. 2003). We selected nearby A0V star, HIP 94140 (B=6.26 and V=6.26) and HIP 91315 (B=5.69 and V=5.74) as telluric standards for atmospheric correction. Observations were made with the LXD_long mode with a slit of 0.″8×15″, providing spectra covering 1.98–5.3 μm with R=2500. The sky conditions for all three nights were stable with a typical seeing of ~0.″9. All observations were made using the ABBA nod patterns to remove telescope and sky background. An integration time of 60 s was used for 8 cycles on the target, resulting in a total on-target integration time of 960 s for each of the epochs. Internal arc lamps were used for wavelength calibration, along with sky lines at the longer wavelengths. Spectral flat fields were taken with internal lamps, as described in Rayner et al. (2003).

SpeX data were reduced using the SpeXtool software package (Cushing et al. 2004) following the standard reduction procedure (Vacca et al. 2003). The target is too faint to have good signal-to-noise spectra at the longest wavelengths (order 4); we then trimmed any data points longwards of 3.8 μm. For each epoch, multi-cycle spectra were then combined using the robust weighted mean method. We found no convincing flux variability (above ~10% level) among the three epochs. We then combined the three epoch spectra by weighted average and smoothed to R=200 for assessing the general shape of the infrared excess as shown in Figure 3. All three IRTF observations were conducted between the two observing windows of the NEOWISE Reactivation project in 2020. The W1 and W2 band fluxes of the source show only small changes (<3%) between these two windows. Figure 3 displays averages of the two W1 and W2 observations. As the plot demonstrates, the average of the W1 measurements coincides very well with the averaged IRTF spectrum indicating that the absolute calibration of the latter is of good quality.

2.4 Optical monitoring

The emission measured in the IRAC bands comes partly from the dust disc and partly from the photosphere of the star. It is therefore also important to monitor the variations in the stellar brightness over the studied period. For this purpose, we conducted optical photometric observations using Bessel $BV(RI)_C$ filters at the Piszkéstető Mountain Station of Konkoly Observatory (Hungary) using the 60/90/180 cm Schmidt telescope equipped with a 4096×4096 pixel Apogee Alta U16 CCD camera. The camera had a pixel scale of 1.″03 and a field of view of 1.°17×1.°17. Over the period covered by our *Spitzer* monitoring project we obtained 127 imaging blocks during 123 nights. The average cadence was 6.8 days. In each imaging block, typically five images were taken with each filter. We reduced the images in IDL following the standard processing steps of bias and dark subtraction and flat-fielding. We calculated aperture photometry for the target and several comparison stars using an aperture radius of 5 pixels and sky annulus between 20 and 40 pixels. We used on average 170 comparison stars within a half degree radius of TYC 4209. We took standard magnitudes for the comparison stars
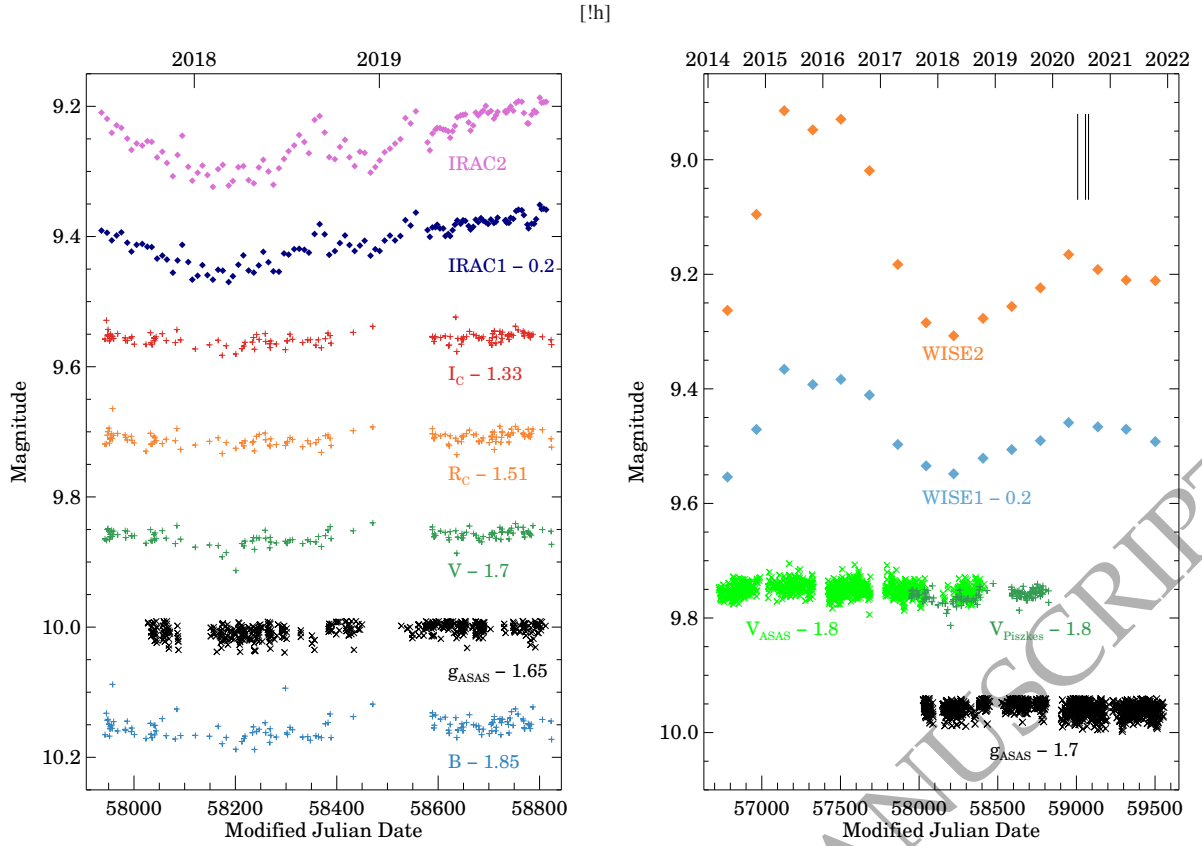
[!h]

Figure 4. Optical and infrared light curves of TYC 4209, during the *Spitzer* monitoring campaign, between 2017 and 2019 (left panel) and during the NEOWISE Reactivation mission between 2014 and 2022 (right panel). For clarity, the light curves are shifted along the y axis by the indicated magnitudes. The utilized photometric data sets are described in Sect. 2. Black vertical lines in the right panel mark the epochs of our IRTF/SpeX observations.

from the APASS9 catalogue (Henden et al. 2015) and converted the Sloan $g'r'i'$ magnitudes to $R_C I_C$ by spline interpolating in the comparison stars' SEDs for the effective wavelength of these filters. We obtained the calibration factor by fitting a linear colour term for the $V - R_C$ colour and iterating until the photometry of the science target converged. Typical rms scatter of the photometry are 0.009 mag in the B band and 0.006 mag in the $V R_C I_C$ bands. In the data analysis we utilized the daily average of the obtained magnitudes in each filter. The measured B, V, R_C, I_C light curves together with the IRAC1 and IRAC2 photometric data (in magnitudes) are displayed in Figure 4 (left).

TYC 4209 was covered by the All-Sky Automated Survey for Supernovae (ASAS-SN, Shappee et al. 2014; Kochanek et al. 2017) photometry survey, providing V band data between 2012 April and 2018 October, and g band observations since 2017 October. The latter data (see Fig. 4, left) similarly to our observations from Piszkéstető, cover well the period of the *Spitzer* IR monitoring with a median cadence of 1.75 days. The V-band measurements provide information about stellar variability in the first five years of the NEOWISE Reactivation mission, allowing its comparison with the changes seen in the $W1$ and $W2$ bands in that period (Fig. 4, right).

3 DATA ANALYSIS

3.1 Optical variability

Using the available optical light curves (Sect. 2.4) we explored the stellar variability and investigated its possible contribution to the observed changes in the mid-infrared bands. As Figure 4 (left) demonstrates, during the *Spitzer* monitoring the system exhibited much larger amplitude changes at 3.6 and 4.5μm than in the optical bands. The standard deviation of the B, V, R_C, and I_C light curves are 0.013, 0.010, 0.010, and 0.009 mag, respectively, while for the corresponding part of the ASAS g-band photometry, $0.^{\rm m}009$ is obtained. This indicates that the stellar brightness is stable within ~1%. The contribution of the star to the total flux is 56–63% and 38–43% at 3.6 and 4.5μm, respectively. So even if the variations of the star at 3.6 and 4.5μm are similar in amplitudes to those in the optical bands, they are negligible compared to the mid-infrared changes observed with amplitudes of ~11% and ~13%, respectively. As Figure 4 (right) shows, the same is particularly true for the variations observed between 2014 and 2018: the changes in the star's V band photometry ($\sigma_{V_{ASAS}} = 0.^{\rm m}013$) are dwarfed by the ones seen in the $W1$ and $W2$ bands.

In addition to ground-based optical data, space photometry is also available for TYC 4209 thanks to the Gaia and the Transiting Exoplanet Survey Satellite (TESS, Ricker et al. 2015) space telescopes. TYC 4209 was observed in 10 sectors (each ~27 days long) during Year 2 of the TESS mission in the time range between 2019 August 15 (MJD 58711.4) and 2020 July 4 (MJD 59035.1), the first

65 days of this data series overlap with the *Spitzer* light curves. By analyzing the whole TESS data set, we revealed a modulation with a period of 5.07 days and an amplitude of 0.0032 magnitude, attributed to starspots and stellar rotation (Moór et al. 2021). We found some weaker peaks around the dominant one in the Fourier spectrum and interpreted them as signs of differential rotation. The effect of rotational modulation can also be detected in the ASAS light curves. By calculating the generalized Lomb–Scargle (GLS) periodograms of the *V*- and *g*-band data (Zechmeister & Kürster 2009) using the IDL implementation of the publicly available code[9], we found significant peaks at ∼5.13 d and ∼5.04 d, with false alarm probabilities (FAPs) of 1×10^{-4} and 8×10^{-9}, and with amplitudes of 0.0035 and 0.0042 mag, respectively. There is an additional 29.5-day period in the *V* light curve, but we also found that period in the ASAS data of most surrounding stars, implying that it is probably an instrumental artifact caused by the lunar phase, as it is identical to the length of the synodic month. According to Gaia EDR3 (Gaia Collaboration et al. 2020), TYC 4209 was observed photometrically at 355 epochs in the *G* band and at 41 epochs in the $G_{\rm BP}$ and $G_{\rm RP}$ bands. These observations were conducted between 2014 July 25 and 2017 May 28, during a period when the object significantly brightened and then faded in the mid-IR (Fig. 4, right). Although individual data points are not available, the relative standard deviation of the multi-epoch Gaia photometric data can be calculated as $100\times\sqrt{N_{\rm obs}}\frac{\sigma_f}{f}$ based on the number of measurements ($N_{\rm obs}$) and the flux (f) and flux error (σ_f) listed in the EDR3 catalogue. This yields relative standard deviations of 0.77, 0.83, and 0.48% for the *G*, $G_{\rm BP}$ and $G_{\rm RP}$ data sets, respectively. This result also indicates that the optical brightness of the star was very stable over the given period.

Interestingly, the optical light curves between 2017 and 2019 (Fig. 4, left) show a trend that follows the changes observed in the mid-infrared wavelengths, albeit with very low amplitude. We applied the locally weighted scatterplot smoothing (LOWESS) algorithm to the *V*-band light curve to find the trend and then interpolated it to the epochs of the *Spitzer* measurements. In Fig. 5 we display scatter plots of IRAC1 and IRAC2 photometry against this *V*-band trend. In the period between MJD 58400 and 58585, practically there is no *V*-band photometry available, making the trend estimate unreliable, therefore *Spitzer* measurements from this time range have not been used in the plot. The figure indicates a correlation between the mid-infrared and the *V*-band data. The Pearson correlation coefficient between the IRAC1 and the *V*-band photometry is $r_{\rm IRAC1-V} = 0.9$, while for the IRAC2 and *V* data pairs we obtained $r_{\rm IRAC2-V} = 0.89$. Comparing the other optical band measurements with the *Spitzer* data also indicates significant correlations. Considering IRAC1 observations, the correlation coefficients between them and data measured with the *B*, $R_{\rm C}$, and $I_{\rm C}$ filters are 0.91, 0.89, and 0.86, respectively, while for IRAC2, 0.88, 0.89, and 0.88. By applying linear regression for the data pairs using an ordinary least squares bisector method (Isobe et al. 1990) we obtained slope values of 4.7±0.4, 5.6±0.4, 7.5±0.6, and 8.3±0.8 for IRAC1 versus *B*, *V*, $R_{\rm C}$, and $I_{\rm C}$ data, and 5.6±0.5, 6.8±0.6, 9.1±0.8, and 10.1±0.9 for the relations between IRAC2 and the same optical photometry. The mid-IR brightness variations of the system are likely related to the changes in the emitting area of the dust disc (Moór et al. 2021, Sect. 4.2). Based on the above relations, the optical brightness variations of the system are correlated with this, and when the disc is brighter in the mid-IR, the system becomes brighter and bluer at optical wavelengths. A possible explanation is that these optical changes
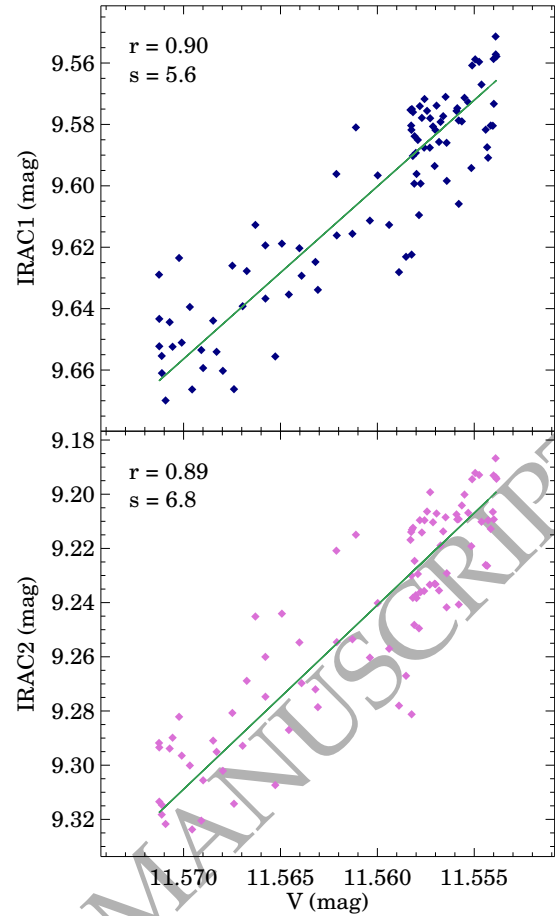
Figure 5. Scatter plots of the measured V and IRAC1 (top), IRAC2 band (bottom) photometric data with the best fit lines. Values of the Pearson correlation coefficients (*r*) and the derived slopes (*s*) of the fitted lines are also shown.

are related to the scattering of starlight by the fresh dust particles. However, the observed relationship does not seem to be as strong in all periods. Comparing the ASAS *V* photometry with the *WISE* half-annual data yields a somewhat weaker correlation with coefficients of $r_{\rm W1-V} = 0.69$, and $r_{\rm W2-V} = 0.68$. In addition, the resulting slopes are much larger, 15.6±2.6 for *W*1 and *V* data pairs and 29.4±4.8 for *W*2 and *V* data. Although these WISE bandpasses are not identical to the IRAC bandpasses, the *W*1 (*W*2) filter is very similar to the IRAC1 filter (IRAC2). So the difference in the slopes may not be due to the difference in the filters, but to the fact that the relationship in the earlier 2014–2018 period was different from the period covered by the *Spitzer* measurements. If the observed effect is indeed related to starlight scattered by dust grains, then it suggests the presence of different dust populations in the two periods (Sect. 4.3.1).

3.2 General disc properties

Figure 6 shows the spectral energy distribution (SED) of TYC 4209 with all available near- and mid-infrared photometric and spectroscopic observations. Comparing the best fitting Kurucz model of the stellar photosphere (taken from Moór et al. 2021) with these data, indicates that the object exhibits excess at all wavelengths longward of 2 μm. To estimate the basic disc properties, in Moór et al. (2021)
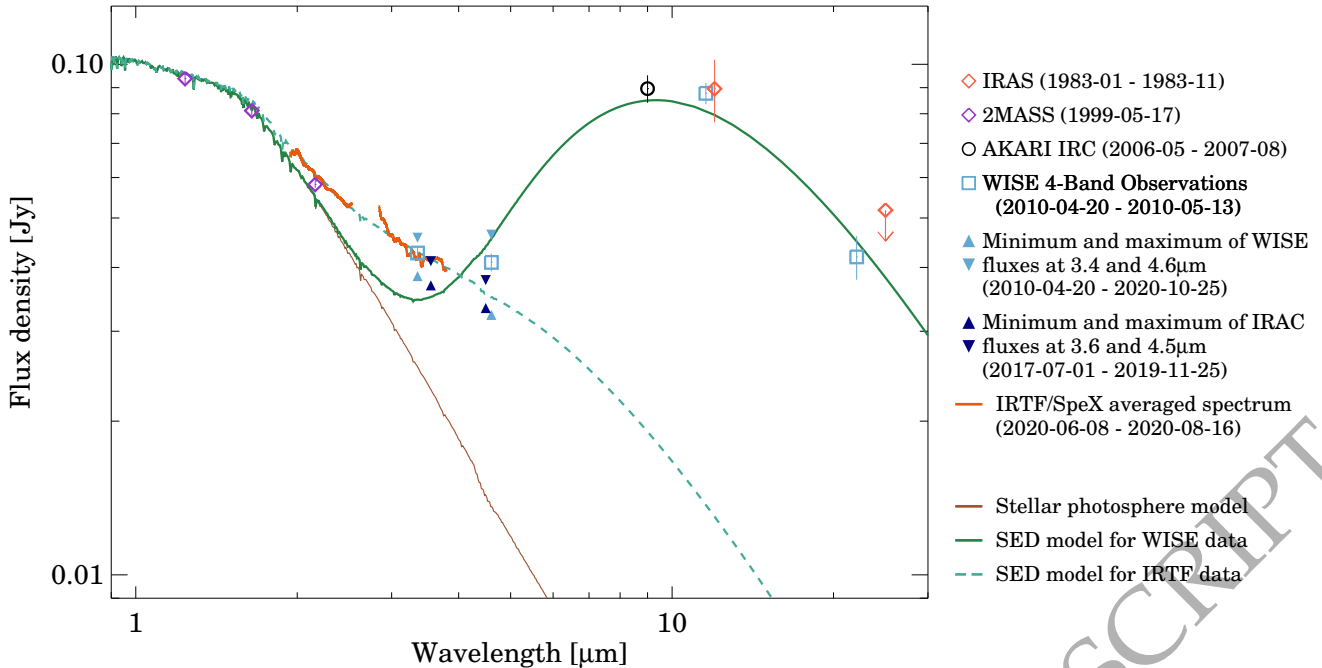
Figure 6. Spectral energy distribution of TYC 4209. The green solid and dashed curves show the best fitting SED models to the *WISE* four band data measured in 2010 (Moór et al. 2021) and to the IRTF spectrum in 2020 (Sect. 2.3), respectively.

we fitted a single temperature blackbody model (green solid curve in Fig. 6) to the excess measured in the four *WISE* bands during the cryogenic phase of the mission (blue open squares in Fig. 6). This fit yielded a characteristic dust temperature of ~530 K and a fractional luminosity of ~0.07. The applied model is clearly oversimplified. Firstly, most EDDs show strong solid state emission features. TYC 4209 does not have any mid-IR spectral information, therefore, we cannot assess how such features might affect the shape of the SED in our case. Secondly, the single temperature blackbody model significantly underestimates the flux data at 3.4 μm, suggesting the presence of additional hotter dust particles in the disc. Measurements obtained at other epochs also support the latter hypothesis. *WISE* and IRAC data point pairs indicate dust colour temperatures between 760 and 1000 K (Sect. 4.2), while the excess measured by the IRTF spectrum can be fitted very well with a 1040±10 K blackbody model that has a fractional luminosity of 0.04 (Figure 3 and 6).

The minima and maxima of the *WISE* $W1$ and $W2$ band flux data in Fig. 6 show that this warm component displayed large brightness variations over the last decade. The 3.4 μm *WISE* time-domain data make it clear that the disc in some periods was even brighter at this wavelength than at the time of the IRTF measurement. During these periods, the total infrared luminosity of the disc likely exceeded the 10% of the stellar luminosity. Of the known EDDs, only the warm disc of V488 Per exhibits a higher fractional luminosity (Zuckerman et al. 2012; Rieke et al. 2021; Sankar et al. 2021). TYC 8830-410-1 is comparably dust-rich (Cotten & Song 2016; Melis et al. 2021), and before its fading, a similarly high fractional luminosity was measured for TYC 8241-2652-1 (Melis et al. 2012).

Assuming blackbody grains, the dust temperatures of 1040 K and 530 K correspond to radial distances of 0.09 and 0.33 au from the star, respectively. Obviously, the inferred radii have a large uncertainty, since the measured emission is partly optically thin and partly

optically thick, and the composition and size distribution of the dust is poorly known.

3.3 Variability of the disc emission

At wavelengths longer than 5 μm, data are available for three epochs between 1983 and 2010, from *IRAS* (1983), *AKARI* (2006–2007), and from the cryogenic phase of *WISE* (2010). These measurements do not suggest significant changes in the 9–20 μm range, though because of the sparse sampling, it cannot be ruled out that they were present in the periods not surveyed. For shorter wavelengths (<5 μm), there are measurements from 1999 to 2021. They indicate the presence of a hot dust component in the disc in all studied times. In the earliest 2MASS near-IR observations, there is significant, 3.4 σ excess in the K_s band.

Figure 7 shows the time behavior of the 3–5 μm disc emission between 2010 and 2022. The excess data were computed by subtracting the corresponding photospheric flux densities from the *WISE* (Sect. 2.2) and *Spitzer* IRAC measurements (Sect. 2.1). In the common observing period, the light curves obtained with the two instruments – with different time resolution and with some deviation in the flux levels due to the different filters – show the same trend. The *WISE* data show changes on a longer, annual timescale between 2014 and 2022. As described in Moór et al. (2021), a significant brightening of the disc started sometime in 2014, followed by a roughly constant brightness plateau between April 2015 and April 2016, after which the disc faded, returning to prebrightening flux levels by early 2018. Then the flux of the disc started to increase again at both wavelengths, although more slowly and with lower amplitude than in 2014. The data points after mid-2020 indicate a slow fading of the disc. Our *Spitzer* monitoring project, which run between July 2017 and November 2019, gives a more detailed picture about disc flux variations at 3.6 μm and 4.5 μm in the last part of the long fading
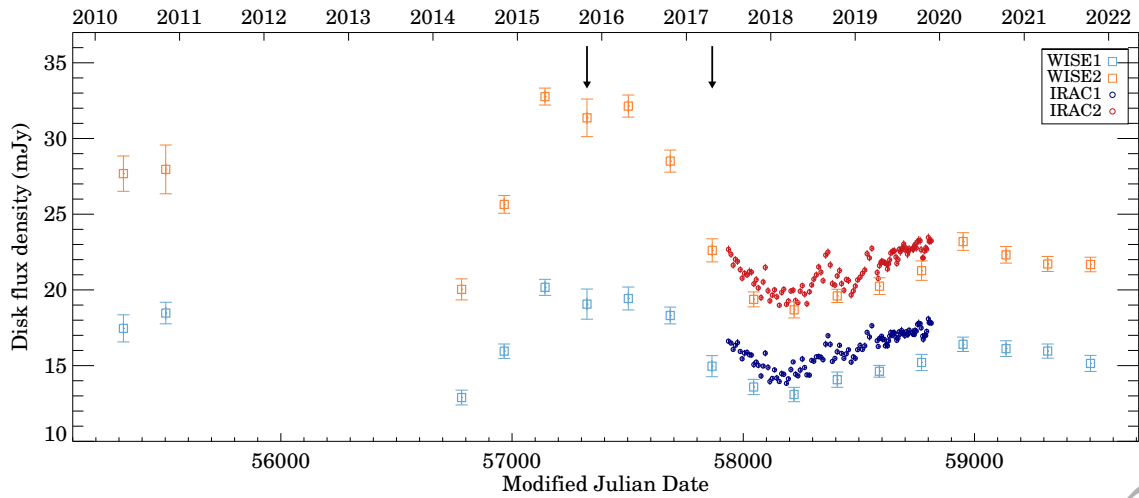
Figure 7. Mid-infrared light curves of the disc fluxes (the measured excess emissions) of TYC 4209 from 2010 to 2020. The plotted semi-annual *WISE* data points were derived by averaging the available good quality single exposure measurements in each available observing window (Sect. 2.2). Arrows mark those observation windows in which significant flux changes have been detected in the single exposure data (Moór et al. 2021).

phase and in the new brightening phase (Fig. 7). At this time the disc exhibited a peak-to-peak flux variation of 26% and 21% at 3.6 μm and 4.5 μm, respectively. The light curves (Fig. 8a) show that rapid, relatively large amplitude variations are superimposed onto otherwise quite smooth changes in the initial phase of the brightening between June 2018 (MJD~58275) and April 2019 (MJD~58580).

The high precision uninterrupted *Spitzer* time-domain data allow us to search for possible periodic modulations in the disc flux changes. For the period analysis we employed three different methods, the Generalized Lomb–Scargle periodogram (GLS, Zechmeister & Kürster 2009), the phase dispersion minimization (PDM, Stellingwerf 1978), and the Weighted Wavelet Z-transform (WWZ, Foster 1996). Prior to these analyses, the general flux trend was subtracted from the light curves (Fig. 8b). For this detrending, we used a LOWESS algorithm with a window of 270 days as implemented in the wōtan package (Hippke et al. 2019). The GLS periodograms (Fig. 8c) were calculated using the IDL version of the publicly available code[10]. For both light curves, the strongest peak on the periodogram is at a frequency of 0.0255±0.0001d^{-1} that corresponds to a period of 39.2±0.2 days. The False Alarm Probabilities (FAPs) of the peaks are 3.2×10^{-4} and 9.9×10^{-4} for the 3.6 and 4.5 μm data sets, respectively, implying that the peaks are real. These FAP values were computed using a bootstrap approach (VanderPlas 2018). The derived amplitudes of the modulation are 0.28±0.05 mJy and 0.35±0.07 mJy at 3.6 and 4.5 μm, respectively. The trend-subtracted light curves folded with the corresponding peak periods, together with the fitted sine curve are displayed in Figure 8d. As Figure 8c shows, the FAPs of the other peaks in the periodograms are higher than 0.1, thus they are probably not real. The PDM method allows to reveal periodic variations even in data showing no sine-like brightness changes. Utilizing its implementation in PyAstronomy[11] (Czesla et al. 2019), we found that the highest power periods for both time series are at ~39.4 days, which is consistent with the results of the GLS analysis.

To check whether the detected period is present over the whole time interval under study, we applied the WWZ algorithm (using a python

based implementation[12]) on the trend-subtracted light curves of the disc. The resulting WWZ maps (Figure 9) show that although the frequency of ~0.025 d^{-1} is present at some level throughout the time series examined, it is much weaker at MJDs from 58280 to 58600. This coincides with the onset of the brightening that is marked by larger amplitude changes. The data points in Figures 8b and 8d that differ most from the GLS model also belong to this interval of time.

Considering the results of the WWZ analysis, the GLS periodograms were calculated separately for the early part of the light curves (MJD: 57935–58300) when the fluxes show a downward trend and for the last part of the time series (MJD: 58580–58850) that are characterized by a relatively smooth upward trend. For the former, a dominant period of 39.8±0.7 d (with a FAP of 3.3×10^{-3}) was found at 3.6 μm and a period of 39.5±0.6 d at 4.5 μm (FAP=1.5×10^{-4}), with amplitudes of 0.37±0.07 mJy and 0.45±0.08 mJy, respectively. By examining the late part of the data, we found dominant peaks at 40.6±0.6 d (FAP=6.1×10^{-6}) and 39.4±0.7 d (FAP=5.1×10^{-4}) on the periodogram, with amplitudes of 0.29±0.04 mJy and 0.32±0.05 mJy in the 3.6 and 4.5 μm data, respectively. The phases obtained in the analyses of the early and late light curve sections are the same within the uncertainties.

To find out more about how long this short term periodic variation has been present, we explored if there was any sign of it in the *WISE* single exposure data. As we noted in Sect. 2.2, these data samples are measured in observing windows with a cadence of 6 months and with their length between 17 and 40 days, they are typically shorter than the period of the observed variation. Moreover, their typical accuracy is well below that of *Spitzer* photometry. Actually, by examining each window separately, we found significant flux changes only in two of them (Moór et al. 2021). Both sets of measurements preceded the *Spitzer* monitoring project (Fig. 7). To test whether the given *WISE* W1 and W2 light curves are consistent with the periodic modulation found in the *Spitzer* data we fitted them with a sine function, where the phase was fixed to the value inferred from the analysis of the early part of the IRAC light curves (MJD: 57935–58300), while the period and amplitude parameters were free parameters. In the

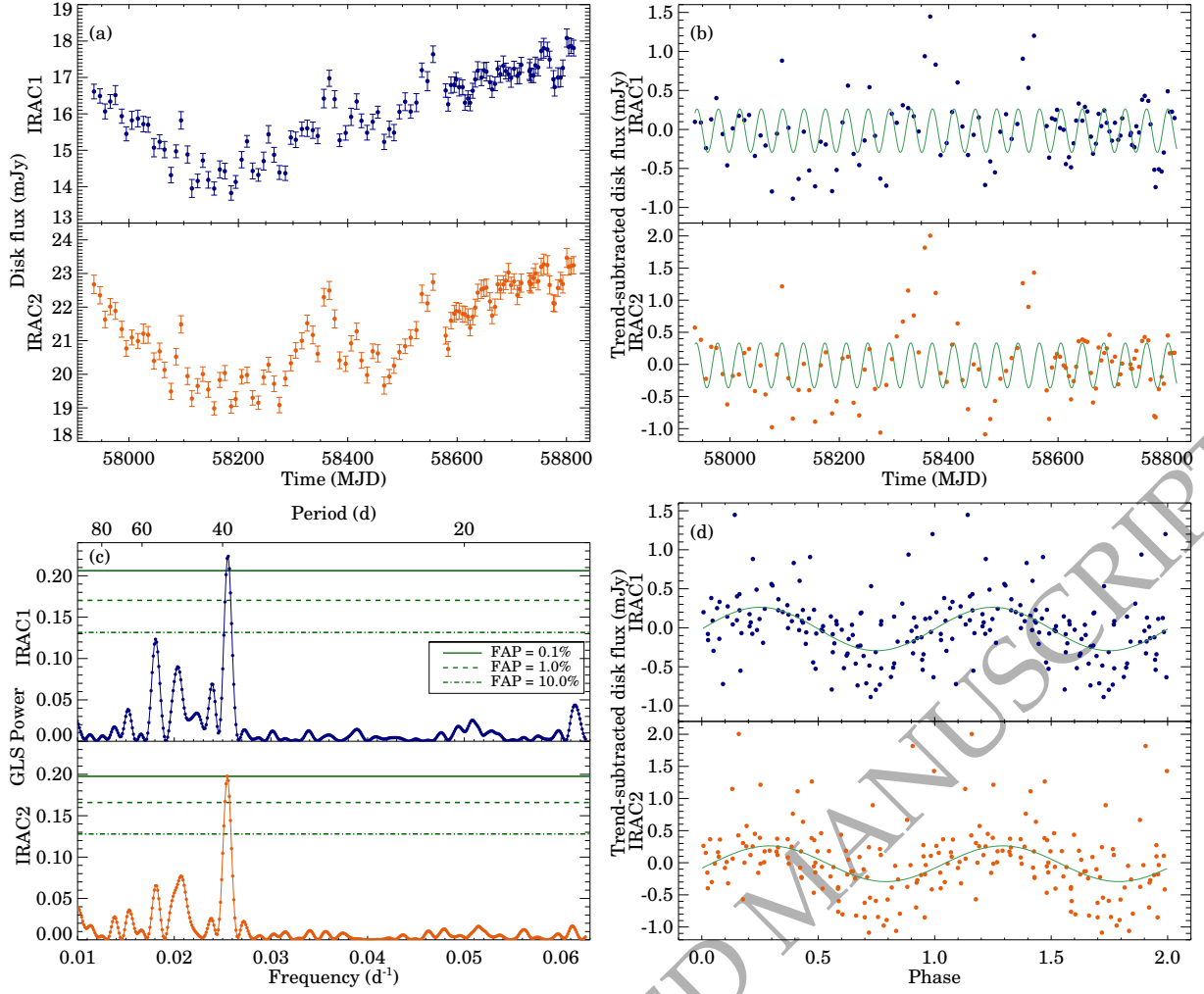**Figure 8.** (a) Light curves of the measured excesses at 3.6μm (IRAC 1) and at 4.5μm (IRAC 2) for the period of the *Spitzer* monitoring project. (b) Light curves of the trend subtracted measured excesses with the best-fit GLS models (green curves). (c) Generalized Lomb–Scargle periodogram of the trend subtracted excesses. (d) Phase-folded light curves of the trend subtracted excesses using the periods associated to the maximum peaks found in the GLS analysis. The green curves show the best-fit GLS models.

fitting, we adopted a constant background, i.e. we assumed that there was no major change in the longer-term trend over the given period. Fig. 10 displays the *WISE* light curves with the best fitted models. For the earlier data set, which preceded our monitoring programme by ∼600 days, we obtain a best period of ∼39 days in both bands, and amplitudes of 1.1 mJy and 1.5 mJy in *W*1 and *W*2, respectively. Due to the short, only 17 days long measurement window, it cannot be ruled out that, despite the reasonably good fit (Fig. 10a), we are in fact only seeing a fading of the object in line with the prevailing long-term trend. What contradicts this is that by the time of the next *WISE* measurements, the disc had become brighter (Fig. 7), in contrast to the strong downward trend observed here. At ∼33 days the other measurement window is particularly long (Fig. 10b). For these observations we find the best fit with a period of ∼42 days, and with amplitudes of 0.5 mJy in the *W*1 and 0.7 mJy in the *W*2 band, respectively. The obtained reasonably good fit and the proximity of the measurement to the monitoring program – last exposure was taken just ∼52 days before the start of the *Spitzer* observations – suggest that the ∼40 days periodic modulation identified there may have already been present during this period.

Using the GLS algorithm, we also investigated whether the ratio

of the IRAC1 and IRAC2 disc fluxes (i.e., the colour temperature of the disc) exhibits periodicity. We found no significant peaks in the periodograms of these data.

4 DISCUSSION

4.1 Grain dynamics

Interactions with the stellar radiation and wind play an important role in the dynamics and removal of smaller solids produced by collisions of larger bodies in the disc. The extent to which a grain is affected by the radiation and stellar wind pressure forces is characterized by the β value, the ratio of these forces to the gravitational force, $\beta = \frac{F_{\rm rad}+F_{\rm sw}}{F_{\rm grav}}$. Assuming that grains are released from parent bodies on circular orbits, particles with $\beta > 0.5$ are blown out from the system on hyperbolic orbits. For compact spherical grains with radius of s and density of ρ, β can be computed as

$$\beta = \frac{F_{\rm rad} + F_{\rm sw}}{F_{\rm grav}} = \frac{3L_*\left(Q_{\rm pr} + Q_{\rm sw}\frac{\dot{M}_{*,{\rm wind}}v_{\rm wind}c}{L_*}\right)}{16\pi GM_*c\rho s}, \tag{1}$$
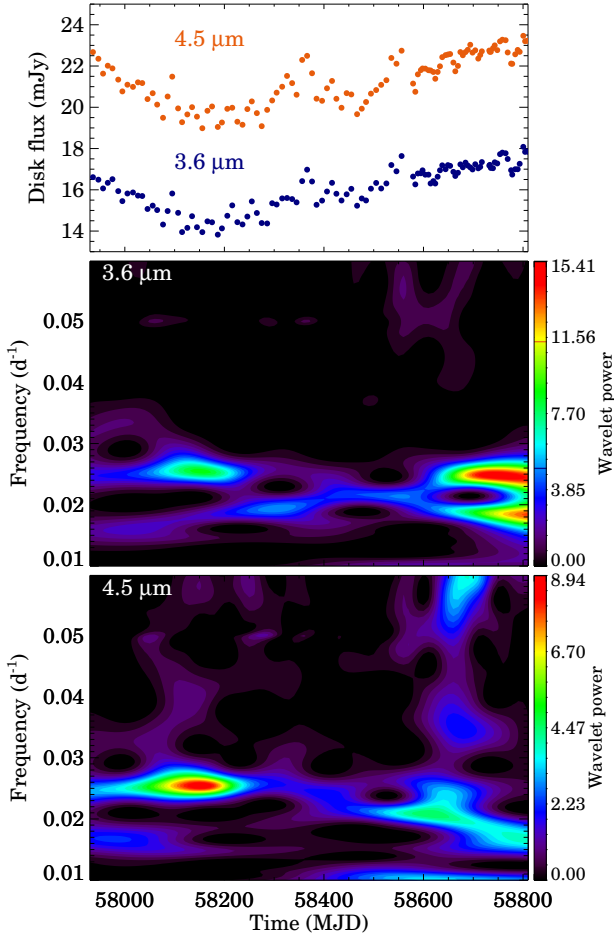
Figure 9. Two dimensional contour maps of the WWZ power spectra computed for the flux density time series derived for the disc at $3.6\,\mu$m (mid panel) and $4.5\,\mu$m (bottom panel). For the sake of easy comparison with WWZ results, the light curves of the disc are also plotted (top panel).

where Q_{pr} is the radiation pressure efficiency, Q_{sw} is the stellar wind coupling coefficient, $\dot{M}_{*,\mathrm{wind}}$ is the stellar wind mass loss rate, and v_{wind} is the stellar wind velocity (e.g. Strubbe & Chiang 2006). The solid black curve in Fig. 11 displays β as a function of grain radius for astrosilicates (Laor & Draine 1993) with a density of 2.7 g cm^{-3} under the influence of radiation pressure alone. The radiation pressure efficiency was calculated from Mie theory using the code developed by Bohren & Huffman (1983). Based on the results, the $\beta > 0.5$ condition holds only for a narrow range of grain sizes between $0.05\,\mu$m and $0.7\,\mu$m. We note that, these are mostly rough estimates, since we do not know the composition of the dust and its possible porosity, which can seriously affect the blowout size (see e.g., Kirchschlager & Wolf 2013; Arnold et al. 2019). In fact, the results from Arnold et al. (2019) show that many realistic grain compositions and structures are more amenable to blowout than the astronomical silicates illustrated in Figure 11.

Young, fast-rotating early G-type stars such as TYC 4209 typically show strong stellar activity and develop substantial stellar wind. By searching the Second ROSAT all-sky survey source catalogue (Boller et al. 2016), we found a source, 2RXS J181703.5+643340, that is located at an angular distance of 15″ from the optical position of TYC 4209, well within the typical positional uncertainty of faint ROSAT sources (Fig. 1). Using the appropriate counts-to-energy con-

version factor quoted in Kashyap et al. (2008), we obtained an X-ray luminosity of $2.7\pm1.0\times10^{29}$ ergs s^{-1}, which is $\sim$120× higher than the average value for our Sun ($2.2\pm1.0\times10^{27}$ ergs s^{-1}, Judge et al. 2003). This implies a moderately strong coronal activity in line with the fast rotation. We note that the coronal activity and the X-ray flux of a star can vary strongly, and since we have one measurement only, it is questionable to what extent the obtained X-ray luminosity can be considered representative for TYC 4209. To assess the possible effect of the stellar wind on the grains, we need to know the wind mass loss rate and the wind velocity (Eq. 1) for which we have no direct measurements. The wind mass loss rate per surface unit is proposed to vary as a function of X-ray flux as $\dot{M}_{\odot,\mathrm{wind}}/R_*^2 \propto F_X^w$ (Wood et al. 2005). Ahuir et al. (2020) argued that the w power-law index falls somewhere between 0.5 and 1.0. Taking these two boundary values, we obtained a mass loss rate range from 14 up to 150 $\dot{M}_{\odot,\mathrm{wind}}$ ($\dot{M}_{\odot,\mathrm{wind}} = 2 \times 10^{-14} M_\odot \mathrm{yr}^{-1}$ is the wind mass loss rate of the Sun) for TYC 4209. As an alternative approach, Johnstone et al. (2015) proposed that the wind mass loss rate can be estimated as $\dot{M}_{*,\mathrm{wind}} = \dot{M}_{\odot,\mathrm{wind}} \left(\frac{R_*}{R_\odot}\right)^2 \left(\frac{\Omega_*}{\Omega_\odot}\right)^{1.33} \left(\frac{M_*}{M_\odot}\right)^{-3.36}$, where R_*, Ω_*, and M_* are the radius, the angular velocity, and the mass of the star. This formula yields $\dot{M}_{*,\mathrm{wind}} \sim 10\dot{M}_{\odot,\mathrm{wind}}$ for our target which is close to the minimum of the mass loss values derived from the X-ray flux. By adopting a wind velocity of 400 km s^{-1}, corresponding to the average wind velocity of the Sun, and assuming $Q_{\mathrm{sw}} = 1$, we recalculated the β ratios by considering the possible effect of stellar wind. As Figure 11 demonstrates, by assuming a mass loss rate of $\dot{M}_{*,\mathrm{wind}} = 10\dot{M}_{\odot,\mathrm{wind}}$ the stellar wind has observable effects only for grains smaller than 0.05 μm, but does not lead to blowout even for those, while in the case of $\dot{M}_{*,\mathrm{wind}} = 150\dot{M}_{\odot,\mathrm{wind}}$ the wind can significantly increase the β of small particles (<0.1 μm) and can even push them out of the system.

The collisional lifetime of the smallest, still bound grains can be estimated as

$$t_{\mathrm{c,bl}}(\mathrm{yr}) = 0.04(r_\mathrm{d}/\mathrm{au})^{1.5}(M_*/\mathrm{M}_\odot)^{-0.5}(dr/r_\mathrm{d})f_\mathrm{d}^{-1}, \qquad (2)$$

where r_d and dr are the disc radius and the disc radial width, respectively (Wyatt et al. 2007). By adopting $M_* = 1.05\,\mathrm{M}_\odot$ (Moór et al. 2021), $r_\mathrm{d} = 0.3$ au, $dr/r_\mathrm{d} = 0.5$, and $f_\mathrm{d} = 0.07$ (Sect. 3.2) this formula yields $\sim$0.05 yr for $t_{\mathrm{c,bl}}$. This calculation supposes an axisymmetric dust distribution, but if the majority of the observed debris is generated in a recent giant impact, then an asymmetric spatial distribution is expected, where most collisions occur at the so-called collision-point (see Sect 4.3 and Jackson & Wyatt 2012). The extremely high collision frequency at this point results in an enhanced collision rate averaged over the orbit of the debris, that is possibly even two orders of magnitude higher than derived assuming an axisymmetric distribution (Wyatt & Jackson 2016). Fragmented particles with $\beta >0.5$, are expelled from the system by the radiation pressure roughly on an orbital timescale. Assuming that they are produced at a radius of 0.3 au this timescale is $\sim$0.16 yr or $\sim$60 days.

Grains are also subject to Poynting-Robertson (P-R) effect and stellar wind drag, which cause the orbiting grains to feel a headwind, lose angular momentum, and drift radially inward. Under the P-R drag, a dust grain revolving on a circular orbit at radius r reaches the star on a timescale of $t_{\mathrm{P-R}}(\mathrm{yr}) = 400\frac{r(\mathrm{au})^2}{M_*(\mathrm{M}_\odot)}\frac{1}{\beta}$ (Wyatt 2005). Adopting an initial orbital radius of 0.3 au, this yields a removal timescale of $\sim$70 yr for grains with $\beta = 0.5$. In debris discs hosted by young, magnetically active late-type stars, the stellar wind drag could be dominant over that of the P-R drag. According to Plavchan et al. (2005), the ratio of the drag times can be estimated as $\frac{t_{\mathrm{P-R}}}{t_{\mathrm{sw}}} = \frac{Q_{\mathrm{P-R}}}{Q_{\mathrm{sw}}}\frac{\dot{M}_{*,\mathrm{wind}}c^2}{L_*}$. By assuming that the $\frac{Q_{\mathrm{P-R}}}{Q_{\mathrm{sw}}}$ ratio of the coupling coefficients is equal
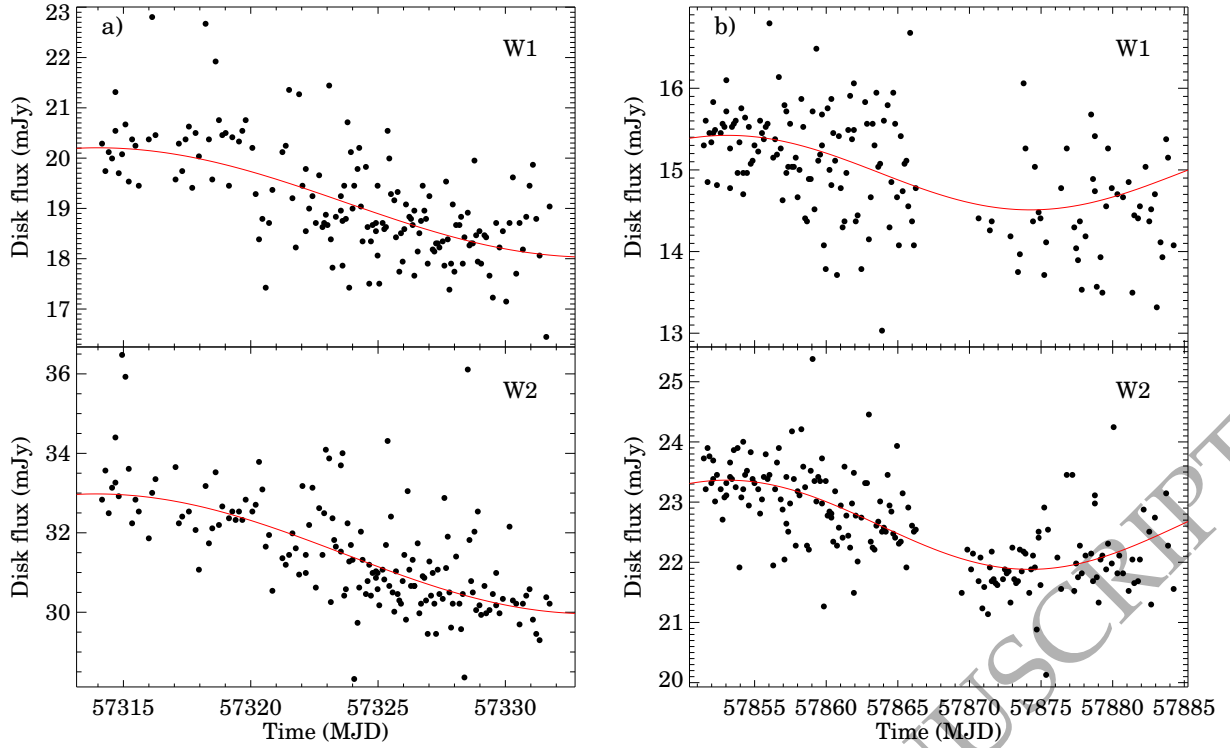
Figure 10. Disc fluxes in WISE $W1$ and $W2$ bands based on single exposure photometric data with the best fit sine model (red line) (see Sect. 3.3).
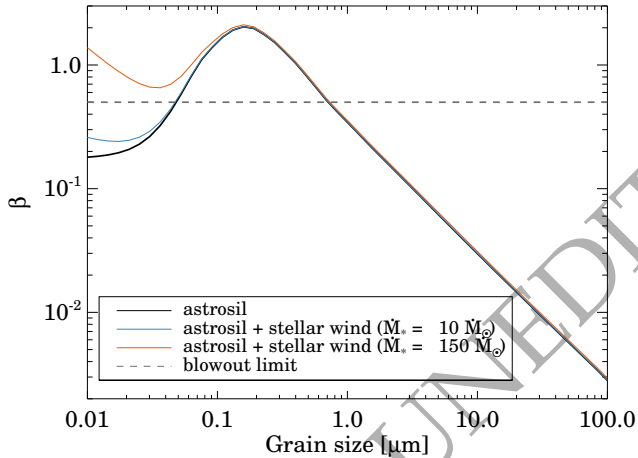

Figure 11. The β ratio as a function of grain size for astrosilicate grains. Influence of the stellar wind pressure force is also explored for wind mass loss rates of $10\times$ and $150 \times \dot{M}_{\odot,\text{wind}}$. The blowout limit of $\beta=0.5$ is shown by a dashed horizontal line.

to 1, and using the maximum value obtained for the wind mass loss rate ($\dot{M}_{*,\text{wind}}=150\dot{M}_{\odot,\text{wind}}$), the timescale of the wind drag is $\sim30\times$ shorter than the P-R timescale. Even this timescale is longer than the collision timescale, indicating that the dust loss is dominated by radiation pressure blowout of small particles, i.e., most particles are destroyed in collisions and expelled by the radiation pressure faster than they can migrate inwards due to the P-R or the stellar wind drag.

4.2 Analysis of the flux changes

In Moór et al. (2021, fig. 9) we analysed the *WISE* W1/W2 colour temperature evolution of the TYC 4209 system. For that we converted the W1/W2 magnitudes to flux densities using the official zero point values of the two *WISE* bands. Then we plotted the data points in a linear W1 (Jy) vs. W2 (Jy) diagram. Any distribution of points following a straight line would correspond to a variability in which the W1/W2 colour temperature is constant. The data presentation method somewhat resembles that of the 'flux variation gradient method' used to separate the contributions of an AGN from its host galaxy (see e.g. Pozo Nuñez et al. 2014). The advantage of our method over analysing the temporal evolution of the W1–W2 magnitude difference is that if the observed flux is the sum of more than one emitting components (which is suggested in our case by Fig. 6), then the W1–W2 colour would not give the colour temperature of the variable component but provide some weighted average of the temperatures of the different components, which is less straightforward to interpret.

In the case of TYC 4209, Moór et al. (2021) suggested that before MJD 58000 (mainly corresponding to the 2014–17 brightness maximum) the mid-IR fluxes increased then decreased with a constant colour temperature of T(W1/W2)$\sim$750 K. We interpreted this as the appearance/disappearance of a warm dust population with a constant temperature. We also mentioned that after 2017 this warm component coexisted with a new hotter component that dominated the integrated flux.

Since this analysis, availability of four new *WISE* data points (for 2020 and 2021) and a number of *Spitzer* measurements helped to refine the above picture. For our present investigation we transformed the *Spitzer* fluxes into the *WISE* photometric system by means of the following linear formulae derived by interpolating the *Spitzer* light curves at the epochs of the *WISE* measurements: $F(W1) = 0.904 * F(\text{IRAC1}) + 0.811\,\text{mJy}$, $F(W2) = 0.791 * F(\text{IRAC2}) +$
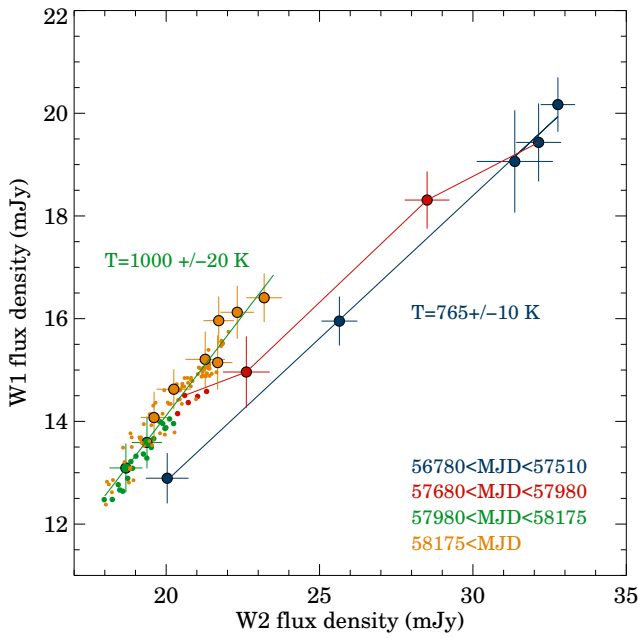
Figure 12. Cross plot of 3.4 and 4.6 μm disc flux densities. Larger circles show the semi-annual *WISE* data measured in the NEOWISE Reactivation mission phase, while the smaller circles denote time domain *Spitzer* photometry transformed into the *WISE* photometric system. The different colours correspond to different time intervals.

1.446 mJy. Fig. 12, which is an updated version of fig. 9 in Moór et al. (2021), shows the flux evolution including all NEOWISE and *Spitzer* photometric points.

In the first part of the studied period, which coincides with the rising branch and the peak of the 2014–2017 brightness maximum (blue circles), the W1 vs. W2 flux distribution follows a linear trend, whose slope corresponds to a colour temperature of 765±10 K. Adopting this value as the physical temperature of the radiating dust grains, the peak-to-peak W2 flux change can be explained by an increase of $0.005\,\text{au}^2$ in the total emitting area. Later, in the last part of the light curve from MJD=57980 until now, the data points again outline a linear locus (green and yellow circles), whose colour temperature, however, is significantly higher, reaching 1000±20 K. This temperature is in good agreement with the value found in our IRTF observation (Fig. 3). In the first section of this period (57980<MJD<58175, green circles) the fluxes decrease until a minimum in early 2018. Using the above high colour temperature value, this drop of flux suggests a change in the emitting area of $\sim 0.0004\,\text{au}^2$. Then, the disc brightens again until MJD=58950, followed by a slow fading phase that is still going on (yellow circles). Within this whole interval (58175–now) the peak-to-peak change in the emitting area is about $\sim 0.0009\,\text{au}^2$. There is also an intermediate time interval between MJD=57500 and 57980, covering the drop from the first peak (2016 Apr) until about 2017 Aug (red circles). In this time interval the disc moved from the 765 K locus toward the hot, 1000 K locus. This may suggest the gradual disappearance of the 765 K dust component, and the parallel building up of the 1000 K emitting dust surface. Interestingly, after an initial build-up of that hot component, its emission dropped until early 2018, then started increasing again.

4.3 Interpretation of the disc variability observed between 2014 and 2021

The episodic dust production leading to the EDD phenomenon is generally attributed to a recent giant impact (Melis et al. 2010; Su et al. 2019). In the following, we will analyse the infrared variations of the disc in the framework of models of giant collisions (Jackson & Wyatt 2012; Jackson et al. 2014; Kral et al. 2015; Watt et al. 2021).

4.3.1 *Variations on yearly timescale*

As Figure 7 shows, between 2014 May and 2015 April the disc flux increased by ∼60% in both W1 and W2 bands. After that, it faded back to its early 2014 flux level over about 2 and a half years. Based on our analysis, the observed variations between 2014 and 2018 are best explained by the appearance and subsequent disappearance of a cloud of fresh dust at a temperature of about 765 K with a minimum emitting area of $0.005\,\text{au}^2$. This is ∼2.5× larger than the emitting area estimated for the 2013 collision in ID8 (Su et al. 2019), but 10× smaller than that obtained for the recent dust production in HD 166191 (Su et al. 2022).

Energetic, high velocity collisions cause a fraction of the impact material to vaporize. As the emerging vapour cloud cools, it rapidly condenses into small spherules having a narrow range of sizes that typically peaks between 0.1 and 10 mm (Johnson et al. 2012). In addition to vapour condensates, the debris material also contains larger boulders which are made of unaltered material. If the fresh dust cloud around TYC 4209 is indeed related to a giant collision, then it likely consists mainly of small spherules that contribute to the IR emission of the disc immediately after their appearance. Right after the collision, the emerging debris is still localised and forms a clump that moves with the progenitor. This clump phase lasts typically no longer than a few orbits (Jackson et al. 2014; Watt et al. 2021). As the optically thick clump spreads due to Keplerian shearing, a spiral structure forms while the brightness of the disc increases rapidly. The spiral structure can then persist for up to 100 orbital periods before, becoming tighter and tighter, it is completely smeared out, leading to a morphology when the debris material is smooth but still highly asymmetric (Jackson et al. 2014). At the same time, spherules are quickly ground down in collisions between each other and with the background disc material. This can further increase the emitting surface for a while, however, as the radiation pressure can expel blowout grains from the emerging optically thin regions, this population disappears and the disc brightness drops.

Assuming that the above inferred minimum emitting area is related to a dust grain population with sizes (s) ranging from radii of 0.7 μm (the blowout limit) to s_{max} and having a power-law size distribution with an exponent of -3.5 ($n(s) \propto s^{-3.5}$), then the mass of these grains is $M_{\text{dust}} \geq 1.8 \times 10^{-6} (s_{\text{max}}/1\text{mm})^{0.5} (\rho/2.7\text{gcm}^{-3})\,\text{M}_\oplus$. The escaping vapour mass is only a fraction of the total mass of the colliding bodies ($f_{\text{vap}} = M_{\text{vap}}/M_{\text{tot}}$). Therefore, the formation of the observed dust population requires the collision of two large bodies with mass equivalent of two spherical bodies with radii of $\geq 78 (s_{\text{max}}/1\text{mm})^{1/6} (1/f_{\text{vap}})^{1/3}$ km. By simulating giant impacts with various parameters utilizing a smoothed particle hydrodynamical code, Watt et al. (2021) obtained f_{vap} values lower than ∼0.2. Adopting this value and an s_{max} of 0.1 mm (thus assuming a maximum size that corresponds the smallest typical spherule size within the range given by Johnson et al. (2012), see above), this formula gives radii of $\gtrsim 90$ km for the case of TYC 4209.

It is worth noting that shock-induced vaporisation requires high impact velocities that depend on the involved planetary material. For

instance forsterite needs an impact velocity exceeding $6\,km\,s^{-1}$, while vaporization of quartz already begins at impact velocities below $4\,km\,s^{-1}$ (Davies et al. 2019). In the case of self-stirring, when the dynamical excitation is linked exclusively to local planetesimals, the typical impact velocity is comparable to the escape velocity of the largest body situated in the region (Weidenschilling 1980). The $4\,km\,s^{-1}$ mentioned above is similar to the escape velocity of Mercury in the solar system. Of course, if other larger planets are present in the system, they may also contribute to the excitation, in which case the local bodies need not to be so large for the proper stirring.

Analysis of the *WISE* and *Spitzer* light curves, as well as our IRTF spectrum, revealed a hotter, $\sim1000\,K$ dust component which may have appeared at some point between MJD=57500 and 57980 when the previously mentioned, $\sim765\,K$ dust material was still present. As the colder grains are gradually removed, the new dust component became more and more dominant. The brightening of the disc after MJD$\sim$58175 is associated with this hot material. Where might this new dust component have been produced? Based on the higher dust temperature, this could belong to a collision that occurred at a smaller radius than the previous one. However, according to models of giant collisions, it is more likely that a new dust production event occur in roughly the same region as the previous one especially due to the high density region at the collision point (Jackson & Wyatt 2012; Kral et al. 2015; Wyatt & Jackson 2016). In the latter scenario, the warmer temperature can be explained if the size distribution of the new grains are different from that of the previous component. In this case, one possible explanation for the formation of such a new component is that it comes from collisional erosion of larger boulders created in the impact in 2014 (or in an even earlier event). The timescale of this process depends on the density of the disc as well as the size distribution and the size-dependent strength of the boulders. As this population contains much larger bodies, the resulting collision cascade can have a longer lifetime than in the case of the vapour component (Su et al. 2019).

An unsolved aspect of this scenario, however, how particles, formed during the fragmentation of boulders, can be so different from the previous dust population. Alternatively, it is possible that this hotter material, or at least a fraction of it, is related to dust forming in optically thick regions of the disc. Shielded from the stellar radiation, inside these regions very finely ground particles can form as a result of frequent collisions. As the clump material evolves to become optically thin, these grains can contribute to disc emission (Su et al. 2020). The fate of such tiny particles depends strongly on the weakly constrained strength of the stellar wind (Sect. 4.1). If the wind mass loss is large, small particles can be quickly repelled from the system under the combined effect of wind and radiation pressure. If the wind is weaker, however, it is possible that their dynamics is more controlled by drag forces and thus they can survive for a longer time (even up to a few decades) as they migrate inwards. This scenario may better explain the different behaviour of the new dust. Interestingly, for the specific time period we also observed a correlation between the optical and mid-IR brightness variations: when the disc was brighter in the mid-IR, the system became brighter and bluer at optical wavelengths. This correlation found to be weaker in the period when the colder dust component was dominant between MJD 56780 and 57680 (Sect. 3.1). If this phenomenon is related to the scattering of starlight by the emerging grains, as we suggested (Sect. 3.1), then it may also indicate that this hot dust population is significantly different from the previous one in terms of size distribution and/or basic geometry.

The slow brightening of the disc starting from MJD$\sim$58175 is interrupted twice by periods characterized by more violent changes.

The two sharp peaks, at MJD=58366 and 58556, are associated with rapid flux increases of 10 and 7%, respectively, followed by rapid fading. These dust releases might be related to smaller collisions, whose optically thin dust product is removed after 1–2 orbits under the influence of the stellar radiation pressure.

4.3.2 Periodic modulation

On top of the annual timescale flux changes, our *Spitzer* observations revealed a shorter-term light curve modulation with a period of $\sim$39 days. Using the full data set, our analysis yields modulation amplitudes of 0.28±0.05 and 0.35±0.07 mJy at 3.6 and 4.5 μm, respectively. At the longer wavelength, the obtained amplitude corresponds to 1.6% and 1.0% of the average disc and the average total fluxes. No variations with similar periods were found in the star's optical light curves, and even the amplitude of the detected rotational modulation is found to be $\sim$0.3% of the stellar flux (Sect. 3.1). The cause of the periodic changes detected in the mid-IR, therefore, could not be the star. By fitting the amplitudes with a blackbody we obtained a temperature of 930±290 K. With this temperature, at the distance of TYC 4209, the observed amplitude at 4.5 μm can be reproduced by an emitting region having a size of $\sim7.5\times10^{-5}\,au^2$, which is roughly equivalent to the size of the Solar disc. Such a large change over such a short period of time can obviously be related to the circumstellar material only.

Actually, the specific disc geometry after a giant collision can offer a natural explanation for the observed flux modulation. The orbits of the newly formed particles must pass through the point where the impact happened, thereby causing a substantial density enhancement at this so-called collision point. Since orbits of debris must also move through the orbital plane of the progenitor, another dense region, the anticollision line, is also formed on the opposite side of the star from the collision point (Jackson & Wyatt 2012). At these special locations, the debris passes through narrower regions, and due to the high optical thickness, this can lead to periodic flux variations (Jackson et al. 2014; Su et al. 2019) whose amplitude and consequently detectability depends on the distribution of the grains' orbital parameters. Observable oscillations occur only for sufficiently narrow distributions of semimajor axes, eccentricities, and inclinations (Watt et al. 2021). The enhancement of the density contrast at the special regions may be different, with the collision point becoming more dominant as the σ_v/v_{Kep} ratio increases (Jackson et al. 2014). In a disc with edge-on or nearly edge-on geometry, an optically thick impact debris cloud, that becomes more elongated over time, exhibits variable emitting cross sections as it orbits. This can also cause flux modulations (Meng et al. 2014; Su et al. 2019). Unless the collision occured halfway between the disc ansae or at the disc ansa, such a configuration results in multiple periodicity in the light curves. In the case of TYC 4209, however, we see only a single period in the data. Moreover, the lack of detectable eclipses in the optical light curves suggests that the disc is probably not perfectly edge-on. Therefore, in the following we adopt a scenario in which we consider only the possible oscillation associated with the collision/anti-collision points. Depending on the density contrasts of these specific regions, the detected single period may be half of the true orbital period, or corresponds exactly to it (if only the oscillation related to the collision point can be detected). While a 39-day orbital period indicates a collision at 0.23 au, an 78-day orbital period would correspond to a radius of 0.36 au. None of these radii are in contradiction with the rough estimates on the disc location inferred from the SED analysis (Sect. 3.2).

P 1121 and ID 8, two EDDs which were targets of five years long

monitoring with *Spitzer*, also display periodic or quasi-periodic variabilities in the mid-IR (Meng et al. 2014; Su et al. 2019). For P 1121, a ~17-day period of variation with an amplitude of 0.08 mJy was observed over the entire studied period. At the distance of TYC 4209, this amplitude would be 0.21 mJy. In the case of ID 8, periodic modulation was seen only for some parts of the studied time interval, with two intermixed periods (26 and 33 days) in 2013 and with a single 10-day period in 2014/2015 (Meng et al. 2014; Su et al. 2019). For the 10 and 26 days periods an amplitude of 0.08 mJy was derived, while the longest period was associated with an amplitude of 0.16 mJy. Scaled to the distance of TYC 4209, these amplitudes would be 0.14 mJy and 0.28 mJy. So, the periods and amplitudes of the flux oscillations detected in the other two EDDs investigated in more detail are quite similar to those seen at TYC 4209.

The periodic modulation is detected mostly based on the high precision *Spitzer* measurements, although in two previous *WISE* observing windows, data hint that this ~39 days period oscillation was already present earlier (Sect. 3.3). According to models, the special geometry associated with the putative collision should already develop shortly after the event, in the spiral phase of the dynamical evolution. Therefore, the appearance of flux modulation even at the time of the earlier *WISE* observing window would not be surprising. The time between the first measurement of that *WISE* window and the last IRAC observation is ~ 1500 days, which is equivalent to ~38 or ~19 orbits for orbital periods of 39 or 78 days. By looking at the amplitudes of the oscillation over the two *WISE* measurement periods and at the beginning and end of the *Spitzer* monitoring program, we see that they tend to decrease with time (Sect. 3.3). Although this finding is in line with theoretical expectations (Watt et al. 2021), it should be treated with some caution since the *WISE* amplitude results are less reliable due to the short observation windows. As our Figures 8 and 9 show, the oscillation can be detected even around the apparent minimum of the disc brightness at MJD~58200. In this respect, the light curve of TYC 4209 is similar to that of P 1121, where the modulation was also observed at the flux minimum (Su et al. 2019). As the flux of TYC 4209 increases again, the modulation signal first weakens and then becomes more detectable again. The upward trend seen in this last part of the *Spitzer* light curve is predominantly attributed to the appearance of a hot dust component (see above). One possible scenario is that this hot material has appeared closer to the star than the previously released debris. However, the periodogram for this time interval still shows only one significant peak with a period of ~39 days (Sect. 3.3). The lack of shorter-period modulation suggests that even if this hot dust is located at smaller radii, it is unable to produce detectable oscillations, for example because it is mostly optically thin.

4.4 The long term history of the disc

In 2010, TYC 4209 showed elevated flux levels in $W1$ and $W2$ bands compared to the ones observed in early 2014 (Fig. 7). This suggests that an additional major collision event may have occurred during or right before this period, whose effect was significantly reduced by 2014. The observed decrease in flux can be explained by the disappearance of ~870 K dust with a minimum surface area of 0.0022 au^2. Assuming that the radiation came from particles with size between 0.7 μm and s_{max} with a size distribution $n(s) \propto s^{-3.5}$, it corresponds to the fragmentation of two bodies with radii of $\geq 59(s_{max}/1\text{mm})^{1/6}(1/f_{vap})^{1/3}$ km. Here we suppose that we were witnessing the early evolutionary phase after an impact event when the vapour condensates dominate the emitting area. If we saw larger boulders being eroded, it would of course indicate a much larger total

mass and larger fragmented bodies. In addition to this, the flux density measured by *IRAS* at 12 μm is in good agreement with the *WISE* 12 μm flux, demonstrating that TYC 4209 possessed similar quantity of dust already four decades ago (Fig. 6). In summary, TYC 4209 has been very dusty for at least 40 years and in that time there have been at least two large collisional events around 2010 and 2014.

Assuming a disc comprised of solids with radii ranging from s_{min} to s_{max} with a size distribution of $n(s) \propto s^{-3.5}$, the total disc mass can be approximated as (Wyatt 2008, eq. 15):

$$\frac{M_{tot}}{M_\oplus} = 2 f_d \left(\frac{r_d}{\text{au}}\right)^2 \sqrt{\frac{s_{min}}{\mu m} \frac{s_{max}}{\text{km}}}/0.37. \tag{3}$$

Using our $f_d = 0.07$ and $r_d = 0.3$ au estimates from the fitting of the WISE data from 2010 (Sect. 3.2), and setting the blowout grain size of 0.7 μm for s_{min} and 90 km for s_{max} (the estimated minimum size of the bodies assumed to be involved in the collision in 2014), this yields a very high disc mass of ~0.3 $M_\oplus$. However, this estimate is hampered by significant uncertainties. Our fractional luminosity estimate (f_d) refers to a period when the disk was brighter – at least at 3–5 μm – possibly due to vapour condensates comprising of small particles only. This overestimation of f_d may be counterbalanced by the fact that the disc may be partially optically thick. For the smallest bodies, we set the blowout dust size derived for astrosilicate grains (Sect. 4.1). Because of the unknown composition and density, this has its uncertainties. Moreover, in the outlined scenario, the majority of collisions occur at the collision point in a presumably optically thick environment, where the rapid fragmentation may result in the formation of very small particles not repelled by the radiation pressure, but are mostly removed by the drag forces on a longer timescale. The potentially most serious uncertainty relates to the size distribution of bodies. Shortly after a giant collision the size distribution of the boulder population can differ severely from the adopted one, expected for a steady-state collisional cascade involving self-similar bodies (Wyatt & Jackson 2016). Thus we need to keep in mind that a steeper size distribution can give orders of magnitudes lower total mass than the above one.

Another possible approach to constrain the amount of solids involved in collisions is to estimate the mass-loss from the available data. Considering the mass of particles just above the minimum grain size in the collisional cascade, $M_{s_{min}} = 5 \times 10^{-9} \rho s_{min} 4\pi r_d^2 f_d$ (Matrà et al. 2017), and the collisional timescale of blowout grains (Eq. 2), we obtain an $\dot{M}_{loss}$ of ~1.6×10^{-5} $M_\oplus$ yr^{-1} and thus a mass loss of ~6.5×10^{-4} $M_\oplus$, i.e. ~4× of the mass of Ceres, over the past 40 years. Since because of the special influence of the collision point, the collisional timescale is likely much shorter than what can be derived from Eq. 2 (Sect. 4.1), and the 40-year lifetime is only a lower limit, the total mass loss was probably much higher. Given that the disc is still present, this also implies that the total quantity of debris generated in putative early giant impact must have been significantly larger.

Considering the quite large disc mass estimates and that the analysis of the mid-IR light curves of the last 10 years indicate at least two major collisions, it is reasonable to assume that what we have seen in the last 4 decades at TYC 4209 is the result of a previous collision involving larger planet-sized bodies. This has resulted in a very large number of fragments, including hundreds kilometer sized bodies, whose subsequent collisions with each other or with the progenitor – likely in the vicinity of the collision point of the original major event – produce newer and newer debris clouds. If this is the case, the orbital radius derived from our study based on the collision in 2014 may give an idea about the approximate location of the original large collision and, if the progenitor was not destroyed, about

its position. Comparing the long term variability of TYC 4209 with that of ID 8 and P 1121, it clearly resembles more the former one whose time-domain data also show evidence of two violent impacts happened with a time difference of a few years only (Su et al. 2019). This latter object is also suspected to originate from a previous large scale embryo-embryo collision (Meng et al. 2014).

4.5 Origin of the disc

In the following, we discuss processes that can lead to giant collisions in the terrestrial region and examine how consistent their expected activity stage is with the age of the TYC 4209 system. Based on the lithium content, rotation, and kinematic properties of TYC 4209 A, the age of the star was estimated to be 275 ± 50 Myr (Sect. 1). For a further, independent age dating of the system, we compared the position of the M-type companion star on a Gaia-based colour-magnitude diagram (M_G vs. $G - G_{RP}$) with those of M-type members of different well-dated stellar clusters, using the plot compiled by Popinchalk et al. (2021, figure 8). We found that the location of TYC 4209 B ($M_G = 11.174 \pm 0.007$, $G - G_{RP} = 1.29 \pm 0.01$) is consistent with those of members of clusters with ages between 100 and 750 Myr (Pleiades, M34, M50, Praesepe, Hyades) but is clearly different from the locus of younger groups, providing a further argument that the system is not younger than 100 Myr.

4.5.1 Giant collision related to terrestrial planet formation

Most planet formation models argue, that after the dispersal of primordial gas, giant collisions among planetary embryos emerging from the protoplanetary disc play an important role in the final assembly of terrestrial planets (Lammer et al. 2021, and references therein). These events are accompanied by the production of copious amount of debris material providing a natural explanation for the EDD phenomenon. Analysis of *Kepler* mission data indicates that 16.5% of FGK-type main-sequence stars host at least one Earth-like planet ($R_{pl} = 0.8 - 1.25_{\oplus}$) with orbital periods up to 85 days and 20.3% of them have at least one super-Earth ($R_{pl} = 1.25 - 2.0_{\oplus}$) in the same orbital period range (Fressin et al. 2013). This shows that stars similar to TYC 4209 commonly host such planets in the region where the collision in TYC 4209 may have occurred.

Simulations of the giant impact phase show that the vast majority of collisions occur in the first few 10 million years after the gas-rich disc dissipates, and even the last events in the series of collisions typically happen within 200 million years (Genda et al. 2015; Quintana et al. 2016). Traces of such giant impacts can be found on most terrestrial planets in our Solar System, the most iconic of which is thought to lead to the formation of the Earth-Moon system (Wyatt & Jackson 2016). Estimates for the epoch of the latter event – which is thought to be one of the last giant collisions between planetary bodies in the Solar System – range between 50 and 200 million years after the condensation of calcium-aluminum rich inclusions (Lock et al. 2020), more likely occurring within 80 Myr (Woo et al. 2022). The migration models of the formation of super-Earths predict resulting configuration with planets in resonant chains. As simulations show, after the dissipation of the gas disc, these chains tend to become dynamically unstable due to gravitational interactions leading to orbital crossing and giant impacts (Izidoro et al. 2021; Esteves et al. 2022). While the last collisions typically happen within 100 Myr, in some cases they can be postponed until 300 Myr or presumably even later (300 Myr was the limit of the simulations in Izidoro et al. 2021). In their recent paper, Melis et al. (2021) proposed such a late-stage

instability as the possible explanation for the formation of the EDD seen in the 600 Myr old TYC 8830-410-1 system.

Thus, the disc observed at TYC 4209 could be the result of a collision related to the formation of Earth-like or super-Earth planets, but if so then it would be an unusually late event in light of current model predictions.

4.5.2 Possible role of internal dynamical instabilities

In systems where giant planets are also present, their possible dynamical instabilities can have a substantial effect on the structure of a planetary system including the formation and evolution of inner rocky planets. A late instability may even change the orbits of rocky planets that have already become stable, causing intersecting orbits and thereby renewing the era of giant collisions. Simulations suggest, however, that such kind of instabilities are more common during the early evolution of the system, happening typically in the first 10 Myr (Bonsor et al. 2013). Several properties of the Solar System suggests that a dynamical instability of outer planets may have had a major role in forming the currently observable configuration of the planetary system (e.g., Gomes et al. 2005; Brasser et al. 2009). When this instability occurred is a matter of debate. While previously, linking to the hypothetical Late Heavy Bombardment event, it was assumed to happen at an age of ~700 Myr (Gomes et al. 2005), more recent results suggest an early instability at <100 Myr (e.g., Morbidelli et al. 2018; Mojzsis et al. 2019). In the latter case, the instability occurred at the same time as the formation of the rocky planets and may have had an effect on that process (e.g., Clement et al. 2018; DeSouza et al. 2021).

4.5.3 Possible role of external dynamical instabilities

Dynamic instability is not only caused by internal effects. By studying known EDD systems, Moór et al. (2021) found that very wide-orbit pairs (with separations >300 au) are significantly more common in old EDD systems than in the normal stellar population. This excess of wide pairs in old EDDs suggests that the companions may have a role in the disc formation. A highly eccentric companion has the potential to trigger a dynamical instability in the planetary system during its pericentre passage. Alternatively, a companion with a properly large inclination with respect to the orbital plane of a planetary system can also result in its significant rearrangement by causing oscillations in the eccentricity and inclination of the planetary bodies via the Kozai-Lidov (KL) mechanism. Both mechanisms can cause collisions between inner planets and a larger body scattered inwards from the outer regions. But the rearrangement that occurs as a result of instability can also be at a level that leads directly to collisions between planets with previously stable orbits in the terrestrial zone.

TYC 4209 has a co-moving, co-distant companion at a projected separation of ~6000 au (El-Badry et al. 2021; Moór et al. 2021), which is an M3.5-type dwarf star with a mass of ~$0.27 M_{\odot}$ (Moór et al. 2021). Because of their long orbital period, orbital parameters of such wide binaries are difficult to constrain. Recent works, based on Gaia astrometric data, found that eccentricities of stellar pairs with separation of >1000 au show a "superthermal" distribution, i.e. they display an excess at high eccentricity values with respect to the "thermal" distribution where $f(e)\, de = 2e\, de$ (Tokovinin & Briceño 2020; Hwang et al. 2022). So this population, to which TYC 4209 belongs, is dominantly highly eccentric. Actually, using astrometric measurements from the Gaia EDR3 catalogue, Hwang et al. (2022) derived an estimate of $e = 0.9$ for the orbit of

TYC 4209 B with 68% lower and upper limits of 0.58 and 1, respectively. Although the nonsignificant proper motion difference of the pair ($\mu/\Delta\mu < 3$) urges caution about the outcome (Hwang et al. 2022), this hints at a quite eccentric orbit for the target.

Even if we assume that the orbital inclination of TYC 4209 B exceeds the critical value with respect to the inclination of a specific third body, the KL mechanism still needs time to have a significant influence at the location of this body. The characteristic KL timescale is $t_{KL} \sim \frac{m_{tot}}{m_B} \frac{P_B^2}{P_C} (1-e_B^2)^{3/2}$, where m_{tot} is the total mass of the system ($m_{tot} = m_A + m_B + m_C$), P_C is the orbital period of the third body, while m_B, P_B, and e_B are the mass, orbital period, and eccentricity of TYC 4209 B, respectively. By assuming a circular orbit for the companion ($e_B = 0$), Moór et al. (2021) concluded that within the system's lifetime it can excite a high eccentricity outward of ∼140 au (considering that the first eccentricity peak is reached at $t_{KL}/2$), i.e. at most it can trigger changes in an extensive outer planetesimal belt, if such a belt exists. In the case of a highly eccentric companion, however, the KL timescale may be shortened and the effects may occur further inwards. For example, by adopting an eccentricity of 0.9 and a semi-major axis of 6010 au (correspondingly to the projected separation) for the orbit of TYC 4209 B, then even a body orbiting at ∼25 au could be affected substantially by the KL mechanism. This could trigger an instability affecting the possible giant planets, eventually causing orbit changes of other inner bodies, e.g. rocky planets (e.g., Carrera et al. 2016).

Formation models of very wide binaries predict initial orbits with high eccentricities (Hwang et al. 2022, and references therein). Because of their large separations, such systems are weakly bound, and therefore, their orbits are strongly perturbed by the Galactic tide, as well as impulses from other passing stars. These effects can increase the eccentricity further, leading to close stellar passages between the companions from time to time (Kaib et al. 2013). Such passages have the potential to trigger a direct dynamical instability in the planetary system eventually leading to collisions in the terrestrial zone. Although the typical timescales of these external perturbation effects are of the order of Gyrs, in some cases it could be only a few 100 million years (Kaib et al. 2013). So this scenario cannot be excluded for TYC 4209 either.

While all of the scenarios outlined above may be at some level feasible for the disc formation, TYC 4209 is still a somewhat odd case because of its age. If the disc is associated with the formation of rocky planets or some internal dynamical instability, it represents a very late phase within this type of models. If we see the result of an instability triggered by some external effect, then – given the characteristics of those scenarios – we can classify it as a relatively early event.

5 SUMMARY

Between 2017 and 2019, using the *Spitzer Space Telescope* we monitored TYC 4209, a system hosting a recently discovered extreme debris disc (Moór et al. 2021), over 877 days at 3.6 and 4.5 μm. Combining these observations with other time-domain mid-IR data, we explored the disc variability on different timescales. The earliest available data, obtained by the *IRAS* satellite, show that the disc was already extraordinarily bright 40 years ago. Based on *WISE* light curves at 3.4 and 4.6 μm the disc exhibited substantial changes between 2010 and 2021, the most significant of which was the brightening and fading between 2014 and 2018, during which its brightness changed by ∼60% in both bands. The *Spitzer* data stream gives a more accurate picture of the fading phase and the subsequent newer

brightening of the disc after 2018, allowing to examine the mid-IR flux change on a timescale of a week. Period analysis of these data revealed a significant oscillation with a period of ∼39 days and amplitudes of 0.28 and 0.35 mJy at 3.6 and 4.5 μm, respectively.

To interpret the observed variations between 2010 and 2021 we adopted the model of giant collisions. We argue that, there were at least two major collision events in the system during this period. The elevated flux levels measured in 2010 imply enhanced dust content which we attribute to a collision that occurred at that time or shortly before and whose effects largely disappeared by four years later. 2014 saw another big dust production event. The subsequent rapid increase in mid-IR flux can be explained by the appearance, and then dynamical and collisional evolution of a copious amount of small spherules, which were formed via quick condensation of vaporized material ejected in the impact. Assuming that these hot (∼760 K) grains formed in a collision of two identical spherical bodies with ≲20% of their material vaporized, we obtained a minimum radius of ∼90 km for these bodies. This dust component gradually disappeared by the end of 2017.

Our analysis also revealed an additional even hotter (∼1000 K) dust component that already appeared when the previously mentioned colder dust was still present and became dominant after its disappearance. The brightening of the disc after 2018 can be mainly attributed to this hotter debris. It is conceivable that this material may also be related to the aforementioned giant impact, either being made of collisional fragments of larger boulders formed in the impact or very fine dust produced in optically thick regions of the debris cloud. This scenario assumes material emerging at a similar radial distance to the previous dust population. The significantly higher temperature of this new component then would indicate grains with very different size distribution from the previous ones. It cannot be ruled out, however, that the higher dust temperature indicates a dust cloud appearing closer to the star instead.

According to models of giant impact, the periodic modulation of the disc flux might be related to the special geometry of the collisional point and the part of the dust ring opposite it (anticollision point). Assuming a circular orbit, depending on the density contrast of these specific regions, the measured 39-day period can imply a dust orbital radius of 0.23 au if the oscillation is associated with the collisional point only, or 0.36 au if both regions have a significant effect on the light curves.

The fact that the disc was already peculiarly dust rich 40 years ago, suggests that the dust production events observed after 2010 may be the aftermath of an earlier more catastrophic collision perhaps involving a planet-sized body. The continuous collisional erosion of different sized bodies ejected in this event might ensure the sustenance of dust, while sporadic collisions between the largest fragments can increase the dust content of the disc significantly from time to time.

TYC 4209 is a fairly bright EDD that has displayed significant changes over the last decade. Due to its fortuitous location in the Continuous Viewing Zone of the *James Webb Space Telescope*, it will be possible to promptly monitor the aftermaths of possible future dust production events using mid-IR spectroscopy, which will provide a unique opportunity to study the associated mineralogical changes.

Propulsion Laboratory, California Institute of Technology under a contract with NASA. This publication makes use of data products from the Wide-field Infrared Survey Explorer, which is a joint project of the University of California, Los Angeles, and the Jet Propulsion Laboratory/California Institute of Technology, and NEOWISE, which is a project of the JetPropulsion Laboratory/California Institute of Technology. WISE and NEOWISE are funded by the National Aeronautics and Space Administration. The publication makes use of data products from the Two Micron All Sky Survey, which is a joint project of the University of Massachusetts and the Infrared Processing and Analysis Center/California Institute of Technology, funded by the National Aeronautics and Space Administration and the National Science Foundation. This work has made use of data from the European Space Agency (ESA) mission *Gaia* (`https://www.cosmos.esa.int/gaia`), processed by the *Gaia* Data Processing and Analysis Consortium (DPAC, `https://www.cosmos.esa.int/web/gaia/dpac/consortium`). Funding for the DPAC has been provided by national institutions, in particular the institutions participating in the *Gaia* Multilateral Agreement. This research has made use of the NASA/ IPAC Infrared Science Archive, which is operated by the Jet Propulsion Laboratory, California Institute of Technology, under contract with the National Aeronautics and Space Administration. We used the VizieR catalogue access tool and the Simbad object data base at CDS to gather data. This project has been supported by the GINOP-2.3.2-15-2016-00003, 2019-2.1.11-TÉT-2019-00056, and K-131508 grants of the Hungarian National Research, Development and Innovation Office (NKFIH). Authors acknowledge the financial support of the Austrian-Hungarian Action Foundation (101öu13, 104öu2). G.C. is supported by the NAOJ ALMA Scientific Research grant code 2019-13B. A.B., Zs.B. and Á.S. are supported by the Lendület Program of the Hungarian Academy of Sciences, project No. LP2018-7/2021 and the KKP-137523 'SeismoLab' Élvonal grant of the Hungarian Research, Development and Innovation Office (NKFIH). Zs.B., L.K., and K.V. acknowledges the support by the János Bolyai Research Scholarship of the Hungarian Academy of Sciences. L.K. acknowledges the financial support of the Hungarian National Research, Development and Innovation Office grant NKFIH PD-134784.

DATA AVAILABILITY

The *Spitzer* data used in this paper are publicly available at Spitzer Heritage Archive (`https://sha.ipac.caltech.edu/applications/Spitzer/SHA/`).

REFERENCES

Ahuir J., Brun A. S., Strugarek A., 2020, A&A, 635, A170
Arnold J. A., Weinberger A. J., Videen G., Zubko E. S., 2019, AJ, 157, 157
Bailer-Jones C. A. L., Rybizki J., Fouesneau M., Demleitner M., Andrae R., 2021, AJ, 161, 147
Ballering N. P., Rieke G. H., Su K. Y. L., Montiel E., 2013, ApJ, 775, 55
Balog Z., Kiss L. L., Vinkó J., Rieke G. H., Muzerolle J., Gáspár A., Young E. T., Gorlova N., 2009, ApJ, 698, 1989
Bohren C. F., Huffman D. R., 1983, Absorption and scattering of light by small particles. Wiley, New York
Boller T., Freyberg M. J., Trümper J., Haberl F., Voges W., Nandra K., 2016, A&A, 588, A103
Bonsor A., Raymond S. N., Augereau J.-C., 2013, MNRAS, 433, 2938
Brasser R., Morbidelli A., Gomes R., Tsiganis K., Levison H. F., 2009, A&A, 507, 1053
Carrera D., Davies M. B., Johansen A., 2016, MNRAS, 463, 3226

Clement M. S., Kaib N. A., Raymond S. N., Walsh K. J., 2018, Icarus, 311, 340
Cotten T. H., Song I., 2016, ApJS, 225, 15
Cushing M. C., Vacca W. D., Rayner J. T., 2004, PASP, 116, 362
Cutri R. M., et al. 2013, VizieR Online Data Catalog, p. II/328
Czesla S., Schröter S., Schneider C. P., Huber K. F., Pfeifer F., Andreasen D. T., Zechmeister M., 2019, PyA: Python astronomy-related packages (ascl:1906.010)
Davies E. J., Root S., Carter P. J., Duncan M. S., Spaulding D. K., Kraus R. G., Stewart S. T., Jacobsen S. B., 2019, in 50th Annual Lunar and Planetary Science Conference. Lunar and Planetary Science Conference. p. 1257
DeSouza S. R., Roig F., Nesvorný D., 2021, MNRAS, 507, 539
El-Badry K., Rix H.-W., Heintz T. M., 2021, MNRAS, 506, 2269
Esteves L., Izidoro A., Bitsch B., Jacobson S. A., Raymond S. N., Deienno R., Winter O. C., 2022, MNRAS, 509, 2856
Fazio G. G., et al., 2004, ApJS, 154, 10
Foster G., 1996, AJ, 112, 1709
Fressin F., et al., 2013, ApJ, 766, 81
Gaia Collaboration et al., 2016, A&A, 595, A1
Gaia Collaboration Brown A. G. A., Vallenari A., Prusti T., de Bruijne J. H. J., Babusiaux C., Biermann M., 2020, arXiv e-prints, p. arXiv:2012.01533
Genda H., Kobayashi H., Kokubo E., 2015, ApJ, 810, 136
Gomes R., Levison H. F., Tsiganis K., Morbidelli A., 2005, Nature, 435, 466
Henden A. A., Levine S., Terrell D., Welch D. L., 2015, in American Astronomical Society Meeting Abstracts #225. p. 336.16
Higashio S., et al., 2022, ApJ, 933, 13
Hippke M., David T. J., Mulders G. D., Heller R., 2019, AJ, 158, 143
Hughes A. M., Duchêne G., Matthews B. C., 2018, ARA&A, 56, 541
Hwang H.-C., Ting Y.-S., Zakamska N. L., 2022, MNRAS, 512, 3383
Isobe T., Feigelson E. D., Akritas M. G., Babu G. J., 1990, ApJ, 364, 104
Izidoro A., Bitsch B., Raymond S. N., Johansen A., Morbidelli A., Lambrechts M., Jacobson S. A., 2021, A&A, 650, A152
Jackson A. P., Wyatt M. C., 2012, MNRAS, 425, 657
Jackson A. P., Wyatt M. C., Bonsor A., Veras D., 2014, MNRAS, 440, 3757
Jayasinghe T., et al., 2018, MNRAS, 477, 3145
Johnson B. C., et al., 2012, ApJ, 761, 45
Johnstone C. P., Güdel M., Brott I., Lüftinger T., 2015, A&A, 577, A28
Judge P. G., Solomon S. C., Ayres T. R., 2003, ApJ, 593, 534
Kaib N. A., Raymond S. N., Duncan M., 2013, Nature, 493, 381
Kashyap V. L., Drake J. J., Saar S. H., 2008, ApJ, 687, 1339
Kennedy G. M., Piette A., 2015, MNRAS, 449, 2304
Kennedy G. M., Wyatt M. C., 2014, MNRAS, 444, 3164
Kirchschlager F., Wolf S., 2013, A&A, 552, A54
Kochanek C. S., et al., 2017, PASP, 129, 104502
Kral Q., Thébault P., Augereau J. C., Boccaletti A., Charnoz S., 2015, A&A, 573, A39
Lammer H., Brasser R., Johansen A., Scherf M., Leitzinger M., 2021, Space Sci. Rev., 217, 7
Landsman W. B., 1995, in Shaw R. A., Payne H. E., Hayes J. J. E., eds, Astronomical Society of the Pacific Conference Series Vol. 77, Astronomical Data Analysis Software and Systems IV. p. 437
Laor A., Draine B. T., 1993, ApJ, 402, 441
Lock S. J., Bermingham K. R., Parai R., Boyet M., 2020, Space Sci. Rev., 216, 109
Mainzer A., et al., 2014, ApJ, 792, 30
Marboeuf U., Bonsor A., Augereau J. C., 2016, Planet. Space Sci., 133, 47
Matrà L., et al., 2017, ApJ, 842, 9
Melis C., Zuckerman B., Rhee J. H., Song I., 2010, ApJ, 717, L57
Melis C., Zuckerman B., Rhee J. H., Song I., Murphy S. J., Bessell M. S., 2012, Nature, 487, 74
Melis C., Olofsson J., Song I., Sarkis P., Weinberger A. J., Kennedy G., Krumpe M., 2021, ApJ, 923, 90
Meng H. Y. A., et al., 2014, Science, 345, 1032
Meng H. Y. A., et al., 2015, ApJ, 805, 77
Mojzsis S. J., Brasser R., Kelly N. M., Abramov O., Werner S. C., 2019, ApJ, 881, 44
Montesinos B., et al., 2016, A&A, 593, A51

Moór A., et al., 2021, ApJ, 910, 27

Morbidelli A., Nesvorny D., Laurenz V., Marchi S., Rubie D. C., Elkins-Tanton L., Wieczorek M., Jacobson S., 2018, Icarus, 305, 262

Olofsson J., Juhász A., Henning T., Mutschke H., Tamanai A., Moór A., Ábrahám P., 2012, A&A, 542, A90

Plavchan P., Jura M., Lipscy S. J., 2005, ApJ, 631, 1161

Popinchalk M., Faherty J. K., Kiman R., Gagné J., Curtis J. L., Angus R., Cruz K. L., Rice E. L., 2021, ApJ, 916, 77

Pozo Nuñez F., et al., 2014, A&A, 561, L8

Quintana E. V., Barclay T., Borucki W. J., Rowe J. F., Chambers J. E., 2016, ApJ, 821, 126

Rayner J. T., Toomey D. W., Onaka P. M., Denault A. J., Stahlberger W. E., Vacca W. D., Cushing M. C., Wang S., 2003, PASP, 115, 362

Ricker G. R., et al., 2015, Journal of Astronomical Telescopes, Instruments, and Systems, 1, 014003

Rieke G. H., Su K. Y. L., Melis C., Gáspár A., 2021, ApJ, 918, 71

Sankar S., Melis C., Klein B. L., Fulton B. J., Zuckerman B., Song I., Howard A. W., 2021, ApJ, 922, 75

Shappee B. J., et al., 2014, ApJ, 788, 48

Sibthorpe B., Kennedy G. M., Wyatt M. C., Lestrade J. F., Greaves J. S., Matthews B. C., Duchêne G., 2018, MNRAS, 475, 3046

Song I., Zuckerman B., Weinberger A. J., Becklin E. E., 2005, Nature, 436, 363

Stellingwerf R. F., 1978, ApJ, 224, 953

Strubbe L. E., Chiang E. I., 2006, ApJ, 648, 652

Su K. Y. L., et al., 2006, ApJ, 653, 675

Su K. Y. L., et al., 2019, AJ, 157, 202

Su K. Y. L., Rieke G. H., Melis C., Jackson A. P., Smith P. S., Meng H. Y. A., Gáspár A., 2020, ApJ, 898, 21

Su K. Y. L., Kennedy G. M., Schlawin E., Jackson A. P., Rieke G. H., 2022, ApJ, 927, 135

Tajiri T., et al., 2020, ApJS, 251, 18

Thureau N. D., et al., 2014, MNRAS, 445, 2558

Tokovinin A., Briceño C., 2020, AJ, 159, 15

Trilling D. E., et al., 2008, ApJ, 674, 1086

Vacca W. D., Cushing M. C., Rayner J. T., 2003, PASP, 115, 389

VanderPlas J. T., 2018, ApJS, 236, 16

Watt L., Leinhardt Z., Su K. Y. L., 2021, MNRAS, 502, 2984

Weidenschilling S. J., 1980, Icarus, 44, 172

Werner M. W., et al., 2004, ApJS, 154, 1

Woo J. M. Y., Brasser R., Grimm S. L., Timpe M. L., Stadel J., 2022, Icarus, 371, 114692

Wood B. E., Müller H. R., Zank G. P., Linsky J. L., Redfield S., 2005, ApJ, 628, L143

Wright E. L., et al., 2010, AJ, 140, 1868

Wyatt M. C., 2005, A&A, 440, 937

Wyatt M. C., 2008, ARA&A, 46, 339

Wyatt M. C., Jackson A. P., 2016, Space Sci. Rev., 205, 231

Wyatt M. C., Smith R., Greaves J. S., Beichman C. A., Bryden G., Lisse C. M., 2007, ApJ, 658, 569

Zechmeister M., Kürster M., 2009, A&A, 496, 577

Zuckerman B., Melis C., Rhee J. H., Schneider A., Song I., 2012, ApJ, 752, 58

van den Ancker M. E., et al., 2021, A&A, 651, L11